THESIS FOR THE DEGREE OF DOCTOR OF PHILOSOPHY

Glass-forming ternary blends: towards stable Polymer Solar Cells

AMAIA DIAZ DE ZERIO

Department of Chemistry and Chemical Engineering

CHALMERS UNIVERSITY OF TECHNOLOGY

Gothenburg, Sweden 2017

GLASS-FORMING TERNARY BLENDS: TOWARDS STABLE POLYMER SOLAR CELLS

AMAIA DIAZ DE ZERIO

© AMAIA DIAZ DE ZERIO, 2017

ISBN 978-91-7597-610-5

Doktorsavhandlingar vid Chalmers tekniska högskola
Ny serie nr 4291
ISSN 0346-718X

Department of Chemistry and Chemical Engineering
Chalmers University of Technology
SE-412 96 Gothenburg
Sweden
Telephone + 46 (0)31-772 1000

Cover: Solution of organic semiconductors used in this thesis on top of a Kofler bench.
Photo by Jonatan Bergek.

Chalmers Reproservice
Gothenburg, Sweden 2017

To my family

Hegoak ebaki banizkio
neria izango zen
ez zuen aldegingo

bainan honela
ez zen gehiago txoria izango.

Eta nik,
txoria nuen maite.

MIKEL LABOA

Glass-forming ternary blends: towards stable Polymer Solar Cells

AMAIA DIAZ DE ZERIO
Department of Chemistry and Chemical Engineering
Chalmers University of Technology
Gothenburg, Sweden

ABSTRACT

The globally increasing use of electricity goes hand in hand with climate change and the gradual depletion of fossil sources of fuel. To address these challenges renewable sources of energy are in high demand. Solution-processable organic solar cells receive particular attention because they promise to combine a set of highly attractive features including low manufacturing cost through large-area and continuous printing, as well as low weight, flexibility and semitransparency. The stability of the light-harvesting organic photovoltaic materials, which typically consist of a finely mixed blend of an electron donor and acceptor, plays a key role in the development of efficient and durable organic solar cells. One essential condition for both high-yield production and a long lifetime is excellent thermal stability. The organic photovoltaic material must be able to withstand high fabrication and operation temperatures.

The aim of this thesis is to explore the use of ternary blends as a tool to improve the often insufficient thermal stability of organic photovoltaic materials. Ternary blends are a relatively new concept within the field of organic photovoltaics. This thesis focuses on blends of a donor polymer and a mixture of the two most common neat fullerenes, C_{60} and C_{70}. Processing of the neat fullerene alloy is facilitated through a highly advantageous increase in solubility, which is found to correlate with the increase in entropy upon mixing. As a result, solar cells with a power conversion efficiency of 6 % are realized, a record for devices based on neat fullerenes. A high tendency for glass formation of polymer:C_{60}:C_{70} ternary blends is found to induce a high degree of thermal stability due to a glass transition temperature in excess of 200°C. Vitrification of ternary blends is discussed in terms of the entropy of mixing, which reduces the rate of both crystal nucleation and growth. Finally, this thesis provides an overview of the current state-of-the-art, discussing both fullerene as well as fullerene-free ternary blends.

Keywords: *organic photovoltaics, ternary blends, thermal stability, fullerenes, glass formation.*

LIST OF SYMBOLS AND ABBREVIATIONS

AM1.5	Air Mass 1.5
AFM	Atomic Force Microscopy
BHJ	Bulk-Heterojunction
C_p	Heat Capacity
CT	Charge Transfer
D:A	Donor:Acceptor
DCB	*o*-Dichlorobencene
DSC	Differential Scanning Calorimetry
EQE	External Quantum Efficiency
FET	Field-Effect Transistors
FF	Fill Factor
GIWAXS	Grazing-Incidence Wide-Angle X-ray Scattering
HOMO	Highest Occupied Molecular Orbital
ITO	Indium Tin Oxide
J_{sc}	Short Circuit Current Density
LSPR	Localized Surface Plasmon Resonance
LUMO	Lowest Unoccupied Molecular Orbital
MPP	Maximum Power Point
NIR	Near Infrared
OPV	Organic Photovoltaic
PCE	Power Conversion Efficiency
POM	Polarised Optical Microscope
PSC	Polymer Solar Cell
SAED	Selected Area Electron Diffraction
T_g	Glass Transition Temperature
TEM	Transmission Electron Microscopy

TTT	Time-Temperature-Transformation
UV-vis	Ultraviolet-visible
V_{oc}	Open Circuit Voltage
XRD	X-Ray Diffraction

LIST OF PUBLICATIONS

This thesis is based on the work contained in the following scientific papers, referred to by their Roman numerals in the text. The papers are appended at the end of the thesis.

Paper I. **Neat C_{60}:C_{70} buckminsterfullerene mixtures enhance polymer solar cell performance**
Amaia Diaz De Zerio, Jonas Bergqvist, Olof Bäcke, Camilla Lindqvist, Renee Kroon, Feng Gao, Mats R. Andersson, Eva Olsson, Olle Inganäs and Christian Müller
J. Mater. Chem. A, **2014,** I (2), 14354-14359

Paper II. **High-entropy mixtures of pristine fullerenes for solution-processed transistors and solar cells**
Amaia Diaz De Zerio, Armantas Melianas, Stephan Rossbauer, Olof Bäcke, Lars Nordstierna, Paul Erhart, Eva Olsson, Thomas Anthopoulos, Olle Inganäs & Christian Müller
Adv. Mater. **2015**, I (45), 7325–7331

Paper III. **Plasmonic Nanospectroscopy Sheds Light on the Thermal Stability of Polymer Solar Cell Blends**
Ferry A. A. Nugroho, Amaia Diaz De Zerio, Camilla Lindqvist, Christian Müller, Christoph Langhammer
Analytical Chemistry. **2017**, 89 (4), 2575–2582

Paper IV. **A fullerene alloy based photovoltaic blend with a glass transition above 200 °C**
Amaia Diaz De Zerio, Armantas Melianas, Ferry A. A. Nugroho, Olof Bäcke, Eva Olsson, Christoph Langhammer, Olle Inganäs and Christian Müller
J. Mater. Chem. A. **2017**, 5, 4156-4162

Paper V. **Glass Forming Acceptor Alloys for Highly Efficient and Thermally Stable Organic Solar Cells (review)**
Amaia Diaz De Zerio and Christian Müller
Manuscript

CONTRIBUTION REPORT

Paper I. Main author and responsible for data analysis. TEM was carried out by Olof Bäcke (Chalmers). Solar cells characterization was performed together with Jonas Bergqvist and Feng Gao (LiU). Wrote the manuscript together with co-authors.

Paper II. Main author and responsible for data analysis. FETs characterization was performed together with Stephan Rossbauer. Solar cells characterization was performed together with Armantas Melianas (LiU). TEM was carried out by Olof Bäcke (Chalmers). Wrote the manuscript together with co-authors.

Paper III. Co-author. Significant contribution in the sample preparation and interpretation of the results.

Paper IV. Main author and responsible for data analysis. Solar cells characterization was performed together with Armantas Melianas (LiU). TEM was carried out by Olof Bäcke (Chalmers). Plasmonic nanospectroscopy was carried out by Ferry A. A. Nugroho (Chalmers). Wrote the manuscript together with co-authors.

Paper V. Planning and designing the review together with co-authors. Wrote the manuscript together with co-authors.

PUBLICATIONS NOT INCLUDED IN THE THESIS

Paper VI. **A new tetracyclic lactam building block for thick, broad-bandgap photovoltaic**
Renee Kroon, Amaia Diaz De Zerio, Scott Himmelberger, Jonas Bergqvist, Olof Bäcke, Gregório Couto Faria, Feng Gao, Abdulmalik Obaid, Wenliu Zhuang, Desta Gedefaw, Eva Olsson, Olle Inganäs, Alberto Salleo, Christian Müller, Mats R. Andersson
J. Am. Chem. Soc. **2014,** 136 (33), 11578–11581

Paper VII. **Molecular Weight Determination by Counting Molecules**
Yuxi Tian, Marina V. Kuzimenkova, Johannes Halle, Michal Wojdyr, Amaia Diaz De Zerio, Per Olof. Larsson, Christian Müller, Ivan G. Scheblykin
J. Phys. Chem. Lett. **2015,** 6 (6), 923–927

Paper VIII. **Mapping fullerene crystallization in a photovoltaic blend: an electron tomography study**
Olof Bäcke, Camilla Lindqvist, Amaia Diaz De Zerio, Stefan Gustafsson, Ergang Wang, Mats R. Andersson, Christian Müller and Eva Olsson
Nanoscale. **2015**, 7, 8451-8456

Paper IX. **Comparison of selenophene and thienothiophene incorporation into pentacyclic lactam-based conjugated polymers for organic solar cells**
Renee Kroon, Armantas Melianas, Wenliu Zhuang, Jonas Bergqvist, Amaia Diaz De Zerio, Timothy T. Steckler, Liyang Yu, Siobhan J. Bradley, Chiara Musumeci, Desta Gedefaw, Thomas Nanna, Aram Amassian, Christian Müller, Olle Inganäs and Mats R. Andersson
Polymer Chemistry. **2015**, 6, 7402-7409

Paper X. **Nano-pathways: Bridging the Divide between Water-Processable Nanoparticulate and Bulk Heterojunction Organic Photovoltaics**
Natalie P. Holmes, Melissa Marks, Pankaj Kumara, Renee Kroon, Matthew G. Barra, Nicolas Nicolaidis, Krishna Ferona, Almantas Pivrikase, Adam Fahya, Amaia Diaz De Zerio, A.L.David Kilcoyneh, Christian Müller, Xiaojing Zhoua, Mats R. Andersson, Paul C. Dastoor, Warwick J. Belcher
Nano Energy. **2015**, 19, 495–510

Paper XI. **On the effect of prevalent carbazole homocoupling defects on the photovoltaic performance of PCDTBT:$PC_{71}BM$ solar cells**
Florian Lombeck, Hartmut Komber, Daniele Fazzi, Diego Nava, Jochen Kuhlmann, Dominik Stegerer, Karen Strassel, Joseph Brandt, Amaia Diaz De Zerio**,** Christian Müller, Walter Thiel, Mario Caironi, Richard Friend, Michael Sommer
Adv. Energy Mater. **2016,** 6, 1601232

Paper XII. **Enhanced Thermal Stability of Polymer Solar Cell Blends Induced by Electron Beam Irradiation**
Olof Bäcke, Camilla Lindqvist, Amaia Diaz De Zerio, Stefan Gustafsson, Ergan Wang, Per M. Kristiansen, Mats R. Andersson, Christian Müller, Eva Olsson
Ultramicroscopy **2017**, 173, 16-23

TABLE OF CONTENT

1

1 Introduction

The global economy is likely to consume more and more energy in the years to come. The world energy consumption will grow 48% by 2040, especially in the non-OECD (Organization for Economic Cooperation and Development) countries, which are driven by strong economic growth.[1,2] The U.S. Energy Information Administration (EIA)[1] has predicted that fossil fuels will continue to supply more than three quarters of the world energy use in 2040. Therefore, even with current policies and regulations, worldwide energy-related carbon dioxide emissions will rise from approximately 36 billion metric tons in 2020 to 43 billion metric tons in 2040.[1] Climate change associated with the use of fossil fuels and the looming worldwide energy crisis has spurred the global community into action. A global agreement ("Bridge Scenario") intends to put the world economy on a more sustainable path by the end of the century.[3] Some of the targets are:

- Increasing energy efficiency in the manufacturing industry, building and transport sectors.
- Progressive reduction in the use of the least-efficient coal-fired power plants and ban of their construction.
- Increasing investment in renewable energy technologies in the power sector from $270 billion in 2014 to $400 billion in 2030.
- Gradual phasing out of fossil-fuel subsidies to end-users by 2030.
- Reduction in methane emissions from oil and gas production.

In the World Energy Outlook of 2016 the EIA has predicted how the energy sector would look like in 2040 if the nations that have ratified the *Paris Agreement*[4] remain on target with regard to the commitments outlined above:

- 37% of power generation from renewables, compared with 23% today.
- 150M electric vehicles on the road, compared with 1.3M today.
- 50% growth in demand for natural gas, overtaking coal in the global energy mix.
- 103.5 million barrels per day (mb/d) oil consumption with 92.5 mb/d in 2015.

- 0.5% average annual growth in energy sector carbon emissions.

The predictions show that CO_2 emissions from the energy sector are not on track to achieve the targeted carbon-neutral economy by 2100.[5] For that reason, significant additional efforts must be made to tackle both global warming and the future world energy demand. The development of new energy technologies based on CO_2-neutral renewable energy sources is a necessity.

Among all renewable energy sources, the sun is the most abundant and unlimited one. *"The amount of solar radiation striking the earth over a three-day period is equivalent to the energy stored in all fossil energy sources."*[6] Thus, there is a huge potential in using the sun's radiation as a sustainable source of energy. In 1767, the Swiss scientist Horace de Saussure built the first solar thermal collector. Almost one century later, in 1839, the French physicist Edmund Becquerel demonstrated for the first time that electricity can be generated directly from solar energy. In 1883 the first working solar cell was created by the American inventor Charles Fritts, achieving 1% efficiency.[7] In 1946 the Bell laboratories patented the first junction semiconductor solar cell,[8] and a decade later the first photovoltaic cell was realised using a silicon *p-n* junction, with an efficiency up to 6%.[9] Since then solar cell technologies have developed tremendously.

One way of classifying solar cells is based on their active, light-harvesting material, which can be divided into three generations according to their state of development and maturity:[10]

- 1st generation. The oldest and most popular type due to its high efficiency of up to 27.6 % (lab based efficiency)[11] and long lifetime of more than 20 years. This class comprises mainly silicon based photovoltaic cells, including single crystal and multicrystalline solar cells.
- 2nd generation. Thin film solar cells, based on materials such as copper indium gallium selenide (CIGS), CdTe and amorphous Si. They are cost effective but offer lower efficiencies compared with 1st generation solar cells (23.3 % lab based efficiency).[11] They can be flexible and light weight.
- 3rd generation. These solar cells include: i) nanocrystal based, ii) organic semiconductor based, iii) dye sensitized, iv) concentrated, and v) perovskite solar cells. These technologies are currently under development, and some of

them are now being up-scaled. Efficiencies have improved substantially during the last few years (22.1% on lab scale)[11] making 3rd generation solar cells now competitive compared with conventional solar cells.

Organic photovoltaics are particularly intriguing due to the low cost of producing organic semiconductors compared with inorganic semiconductors, such as silicon. The ability to manufacture organic solar cells in a continuous printing process, *i.e.*, large-area through rapid coating, makes this technology extremely promising. Moreover, this technology has many other attractive characteristics such as the potential to be flexible and semi-transparent as well as ease of integration in a wide variety of device configurations.

Besides the high efficiencies that crystalline silicon solar cells offer, the price to manufacture them is continuously decreasing, which puts additional demands on 2nd and 3rd generation technologies. The so-called “price per watt”, is the number of dollars needed to buy, install, service and recycle a module that can produce one watt of electricity. Today, the price per watt to produce a high efficiency multi-Si cell (efficiency of >18.4%) is \$0.207 per watt, which is lower compared with the price three years ago (\$0.31 per watt).[12] Ultimately, 2nd and 3rd generation solar cells are projected to be as competitive as silicon-based photovoltaics.

The aim of this thesis is to address a key challenge for organic photovoltaic materials: the poor thermal stability of the active layer donor:acceptor (D:A) blend. Ternary blends are shown to be a unique tool that can be used to induce vitrification of the nanostructure, which represent a new strategy to lower the production cost and improve the thermal stability of such a device. The first two chapters cover a brief overview of polymer solar cells and glass formation in organic solids. The next two chapters describe the use of neat fullerene based ternary blends. Finally, the current state-of-the-art is reviewed, and fullerene as well as fullerene-free D:A_1:A_2 ternary blends which increasingly attract attention, are discussed.

2

2 Polymer Solar Cells

2.1 Solar Energy

Earth is constantly hit by solar radiation and the energy of most photons within the solar irradiance spans the range of 400-1050 nm. A portion of this is absorbed by the atmosphere and the rest reaches the earth´s surface. Solar radiance is defined as the power per unit area incident from the sun at the ground of the earth. For example, the average annual solar radiance in Sweden is 1000-1200 kWh m^{-2}, while in the Sahara the average value can reach 2200 kWh m^{-2}.[13] To compare the performance of different photovoltaic technologies, the AM1.5 standard solar illumination spectrum is used for device characterization (cf. **Figure 2.1**). It corresponds a specific inclination of the module between the sun's position and the zenith (48.2˚). This thesis will focus on solar cells with organics as active materials.

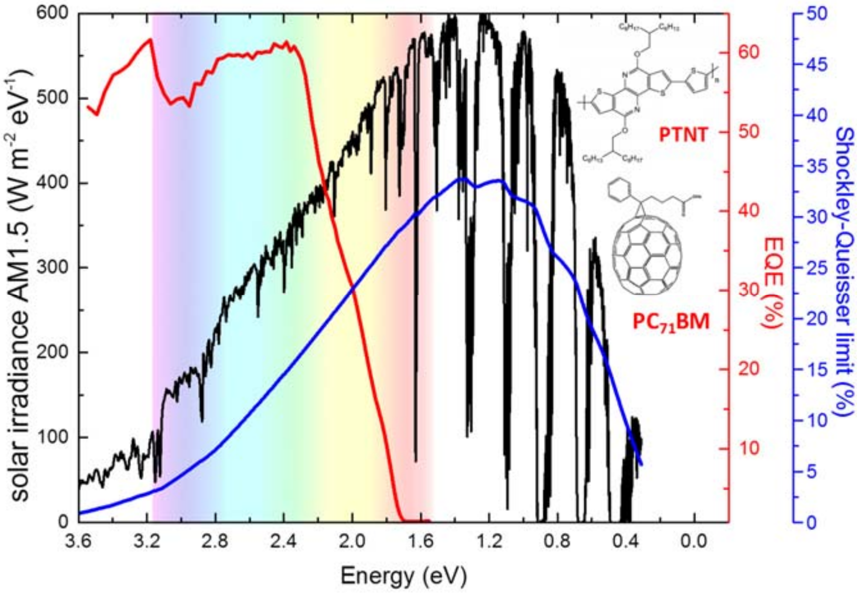

Figure 2.1. *Standardized ASTM G-173-0.3 1.5AM solar irradiation spectrum (black line). EQE spectra of optimized PTNT:PC$_{71}$BM device (red line, reproduced from ref.15) for an active layer thickness of 400 nm. Shockley-Queisser maximum efficiency limit for a single junction solar cell (blue line). The background colour approximately illustrates the visible color part of the spectrum.*

For the choice of semiconductors used in organic solar cells, the electronic structure defines the lower limit of photon energy within the solar radiation, which a device can convert into electricity. The Shockley Queisser Efficiency Limit (SQ limit) refers to the maximum theoretical efficiency of a solar cell using a single p-n junction to collect power at a given absorption edge. The highest possible power output for a single layer solar cell is given by the Shockley-Queisser limit (SQL blue line **Figure 2.1**).[14] The short-circuit current density (*Jsc*) is the photocurrent that the photovoltaic device generates at short-circuit. *Jsc* is predominately given by the number of photons absorbed. The J_{sc} is limited by factors, such as the nanostructure of the device, the active layer thickness and the charge-carrier mobility and lifetime. The reduction of the lower absorption limit increases the number of utilized photons and hence, contributes to the rise of the SQL in the visible range. On the other hand, the bell-shaped SQL suggest a reduction when more lower energy photons are absorbed. This reduction of power output is a result of the reduction of the so called *open* circuit voltage (V_{oc}). The V_{oc} is the voltage output of a solar cell at open circuit condition and is mainly determined by the difference in the highest occupied molecular orbital (HOMO) level of the donor material and the lowest unoccupied molecular orbital (LUMO) level of the acceptor material.

The thickness of the active layer can also affect the performance of an organic solar cell. Thicker active layers have the advantage of increased light absorption, and reduce the risk of pinholes during solution processing. For instance, in **Figure 2.1** the External Quantum Efficiency (EQE) of a PTNT:fullerene blend makes use of over 60% of photons with energy over 2.3 eV when the active layer thickness is ~400 nm, regardless of variations in blend stoichiometry and nanostructure.[15] However, the optimal active layer thickness in most organic solar cells is typically found in the range of 100 nm,[16] due to the limited charge-carrier mobility of organic semiconductors.

2.2 Conjugated polymers

The majority of conjugated polymers, such as polyolefins are insulators and have been used in a large variety of applications ranging from packaging to shopping bags. A breakthrough in the field came in 1977 when Alan J. Heeger, Alan MacDiarmid and Hideki Shirakawa reported a tremendous increase in conductivity in polyacetylene (**Figure 2.2**). By doping the polymer with iodine, the conductivity increase by 7 orders of magnitude (up to 38 S cm^{-1});[17]for this achievement they were awarded the 2000 Nobel Prize in Chemistry. Since then the field of conjugated polymers has grown considerably, and now encompasses a wide range of electrical and electronic applications including organic solar cells.

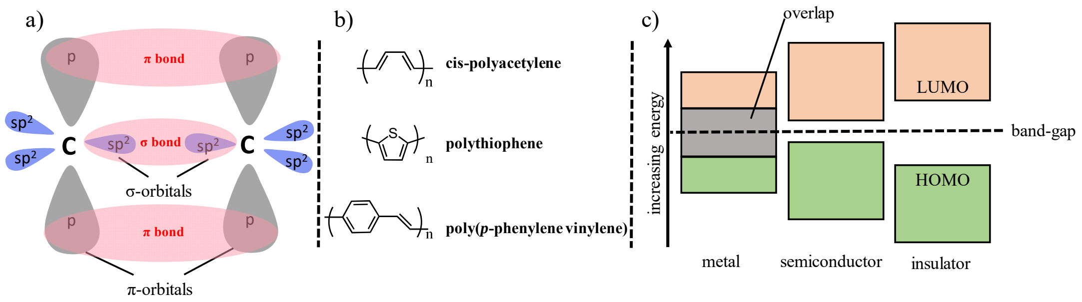

Figure 2.2 *a) Molecular orbitals of a double bond between two carbon atoms, b) chemical structure of cis-polyacetylene, polythiophene and poly(p-phenylene vinylene), c) energy band diagram for conductors, semiconductors and insulators.*

Carbon has four valence electrons that are located in the 2s and 2p orbitals. Orbitals of carbon atoms that form double bonds can be described as sp^2 hybridized, which means that three electrons in the sp^2 orbitals forms a single, or σ-bond and one electron in the p orbital forms a double, or π-bond (**Figure 2.2a**). Alternation of single and double bonds forms an extended π-conjugated system over which the electrons in the π-bonds will be delocalized, allowing them to undergo electronic transitions while the σ-bond preserve the chemical structure of the organic material. The backbone of a conjugated polymer contains a continuous chain of alternating single and double bonds, giving rise to their semiconductor properties. The simplest examples of conjugated polymers are polyacetylene (PA), polythiophene (PT) and poly(*p*-phenylene vinylene) (PPV), among others (see **Figure 2.2b**).

Increasing the degree of conjugation progressively splits the energy levels, resulting in a valence band and a conduction band that are bordered by the HOMO and the LUMO, respectively. The energy difference between the HOMO and LUMO determines the band-gap, which is the minimum energy needed to excite an electron from the HOMO to the LUMO. A higher number of conjugated bonds results in a smaller HOMO-LUMO bandgap of the system, leading to increased semiconducting behavior (**Figure 2.2c**).

A large variety of conjugated polymers exist that have been used as semiconductors with excellent charge carrier mobility and photonic properties for different optoelectronic applications. In this thesis, benzodithiophene-based (BDT),[18,19] thiophene-quinoxaline-based (TQ),[20] and polythiophene-based (PT) materials[21,22] are discussed.

During the last two decades, enormous efforts have been dedicated to the design of donor materials for organic solar cells. The ideal case would be to have a donor material that can be readily synthesized in a few steps. Moreover, the donor material should feature a broad spectral coverage paired with a high absorption coefficient, the right molecular orbital energies to match those of the acceptor and facilitate energy transfer, processability from solution and adequate rheological properties, a sufficiently high hole mobility, and long term stability.

Many donor polymers in organic solar cells are based on aromatic units, which allows introduction of chemical modification for instance via substitution reactions. The stability of aromatic polymers is superior compared to the linear carbon chains found in polyacetylene. In order to increase the absorption spectrum range of a material, a low band-gap is desirable. To achieve a low band-gap material, donor:acceptor (D:A) alternating monomers can be used to increase the double bond character between the aromatic units, thus increasing the delocalization on the polymer and lowering the band-gap.[23]

There are a few aspects that are important to keep in mind when designing a polymer as a potential donor material for organic solar cells:

1. Constitution:

- *Chemical structure of the repeat unit:* most conjugated polymers consist of two components: backbone and side-chains. The conjugated backbone is very important since it determines the electronic behavior of the polymer such as the band-gap and the energy levels. The side-chains influence solubility, reduce thermal transition temperatures and reduce the tendency for aggregation. Through the chemical structure other aspects can be tuned such as:
    - ✓ *Energy levels and band-gap*: Low band-gap polymers harvest more photons from light. However, the open circuit voltage (V_{oc}) can be affected negatively upon lowering the band-gap. Since the V_{oc} is determined by the difference between the HOMO of the donor and the LUMO of the acceptor, the V_{oc} will be reduced by increasing the energy of the HOMO of the donor (see **Figure 2.11**).

    - ✓ *Solubility*: long alkyl side-chains and/or branched side-chains improve solubility in common organic solvents. On the other hand, the introduction of long alkyl or alkoxy side-chains can decrease the glass transition temperature (T_g) of the material,[24] which can be detrimental for the device stability.[25,26]

  - *Molecular weight:* the degree of polymerization influences the solubility, the rheological and mechanical properties, as well as the electronic performance of conjugated polymers. A high molecular weight can improve the photovoltaic performance.[27,28] However, a high chain length reduces the polymers solubility, which complicates synthesis and processing.

2. *Conformation and configuration:*
   - *Conjugation length:* directly depends on the conjugated backbone. The longer the conjugated length, the smaller the band-gap.[29] The change in bandgap saturates as the degree of polymerization increases due to torsion of the polymer backbone.[28]
   - *Regio-regularity:* a high regio-regularity can enhance the ability of the polymer to order, and hence, is considered as a factor that improves the photovoltaic performance in some cases.[30]

3. *Supramolecular structure:*
   - *Crystallinity:* molecular order in the solid state can be described by crystallinity – the volume fraction of crystals. Most polymers are either fully amorphous or semi crystalline in nature. Some materials persist in the liquid crystalline phase once melted. One of the most widely studies semi-crystalline donor polymers is poly(3-hexylthiophene) (P3HT), which gives rise to solar cell efficiencies up to 4% when paired with $PC_{61}BM$ as the acceptor material.[31]

     The effect of crystallinity on the OPV efficiency continues to be a matter of debate. On the one hand, it is well established that higher crystallinity improves hole mobility, and therefore the power conversion efficiency of OPV devices.[32] On the other hand, many non-crystalline conjugated polymers nevertheless are competitive donor materials.

     Qualitative and quantitative analysis of crystallinity can be carried out by a number of characterization methods such as electron diffraction (TEM), X-ray diffraction (XRD), differential scanning calorimetry (DSC), UV-vis spectroscopy or polarized optical microscopy (POM) in some cases. Note that the crystallinity determined by various methods does not necessarily agree with each other. Intriguingly, X-ray diffraction was not able to show strong order within the polymer poly[(4,4′-bis(2-ethylhexyl)dithieno[3,2-b:2′,3′-d]silole)-2,6-diyl-alt-(2,1,3-benzothiadiazole)-4,7-diyl] (PSBTBT) but a crossed-chain structure was observed via high resolution TEM. This polymer yields a high device performance.[33]

Several approaches for improving crystallinity are reported to provide improvement in efficiency. Some of the major techniques are thermal annealing,[34] solvent vapor annealing,[35] and introducing of additives.[36]

One notable approach to taking advantage of the highly-ordered liquid-crystalline structure that some polymers feature, is to anneal at temperatures were the liquid-crystalline phase develops followed by rapid cooling. Poly(2,3-bis-(3-octyloxyphenyl)quinoxaline-5,8-diyl-*alt*-thiophene-2,5-diyl) (TQ1) is an example of a donor material that features a liquid-crystalline phase.[20]

In this thesis, the quinoxaline-thiophene based polymer TQ1 and the widely studied narrow-band-gap fluorothieno-benzodithiophene polymer PTB7 are used (see **Figure 2.3**). Both materials give rise to a promising photovoltaic performance of up to 6-7 % and 9 %, respectively.[18,20,37] One of the biggest advantages (in particular TQ1) is that the polymer can be easily synthetized (in a few steps) and with high molecular weight (up to 100 kg mol^{-1}), which is desirable for up-scaling.

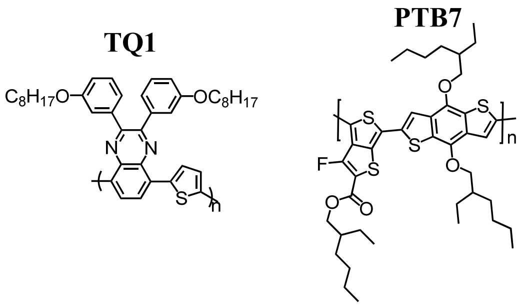

***Figure 2.3**. Chemical structure of TQ1 and PTB7.*

2.3 Fullerene acceptors

The highest power conversion efficiencies in organic photovoltaics are commonly achieved with electron-donating conjugated polymers that are blended with one or more fullerenes, which are the most widely used acceptor materials in OPV. They are also known for being good electron conductors. The next sub-chapter will provide general information about fullerenes and their use as acceptor materials for organic solar cells.

2.3.1 Types of fullerenes

Fullerenes are an interesting class of organic semiconductors that display a high electron affinity (~2.6 eV) and charge carrier mobility (> 1 $cm^2 V^{-1} s^{-1}$).[25,26,38–40] Three decades after fullerenes were discovered,[41] their chemistry is now well established,[42] and many derivatives have been explored for different medical and energy applications such as: *in-vivo* antioxidants,[43] nanocreams,[44] additives for power cable insulators[45] and polymer:fullerene solar cells,[46] among others. With regard to OPV, many compounds have been tested but only a very small selection of fullerene derivatives are found to be promising.

The most commonly investigated un-substituted and substituted fullerenes can be seen in **Figure 2.4**. From left, to right: [5,6]-fullerene-C_{60} (C_{60})[47] is the smallest, most abundant fullerene and has the shape of a soccer ball; [5,6]-fullerene-C_{70} (C_{70})[48–50] has a more rugby-like shape; [6,6]-phenyl-C_{61}-butyric acid methyl ester ($PC_{61}BM$)[51] and [6,6]-phenyl-C_{71}-butyric acid methyl ester ($PC_{71}BM$)[52] are the most frequently used acceptors in OPV, together with indine-C_{60} bisadduct (ICBA) and bis-PCBM ($PC_{61}BM$ bisadduct), which has a LUMO energy level higher than $PC_{61}BM$.[53]

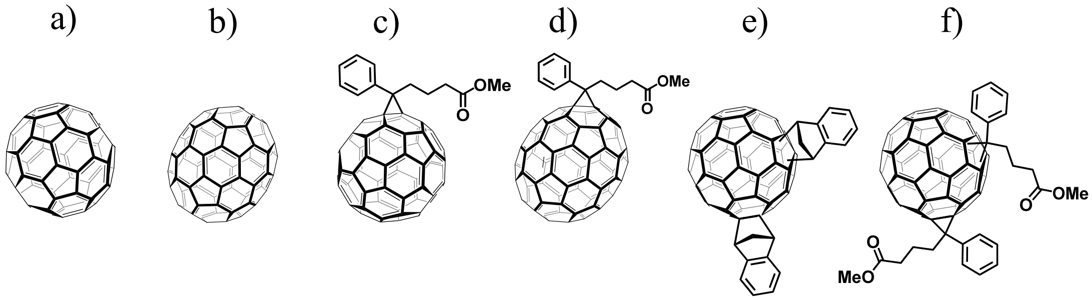

***Figure 2.4**. Chemical structure of neat fullerenes a) C_{60}, b) C_{70}, and fullerene derivatives c) $PC_{61}BM$, d) $PC_{71}BM$, e) ICBA and f) bis-PCBM.*

Pyrolysis and plasma synthesis are among the most used types of fullerene production methods. The former is often viewed as a greener option since it does not produce direct gaseous emissions during the production compared with the plasma technique. The process-flow of fullerene production can be divided into four stages (see **Figure 2.5**):[54]

- *Synthesis:* macroscopic quantities of fullerenes are generated by constant heating and finally evaporation of the carbon source. The raw material obtained from the evaporation is mostly soot and slag. Next to soluble fullerenes, the soot and slag also contains different types of closed-cage carbon structures. The total amount of fullerenes that can be extracted from the carbon soot is less than 30%.

- *Separation and Purification:* The methods for preparation of fullerenes always lead to the formation of a mixture, which consists of C_{60}, C_{70}, C_{76}, C_{78}, C_{84}, and larger close-cage carbon spheres. Their derivatives such as $PC_{84}BM$ have been reported to negatively affect organic photovoltaic performance.[55] In these mixtures, C_{60} is the most abundant, followed by C_{70}. The so-called larger/higher fullerenes, such as C_{76}, C_{78}, C_{84} are present in only small amounts. Separation and purification of C_{60} and C_{70} from the mixture is relatively straightforward and can be done on a large scale.

- *Functionalization:* for OPV applications, fullerenes are normally modified by cycloaddition reactions.[42] This last additional synthesis step is needed to attach a hexahedral substituent (one or two methyl ester functional groups) to the fullerene cage, leading to $PC_{61}BM$, $PC_{71}BM$, bis-$PC_{61}BM$, bis-$PC_{71}BM$ or ICBA. These compounds have a higher solubility, which is advantageous for solution processing. Compounds with a high degree of purity are also necessary to avoid impurity trap states. The functionalization of the bucky balls with butyric acid methyl ester, leads to changes in energy levels. The LUMO level increases, and thus the V_{oc} increases by 0.1 V compared with neat fullerenes when using the same donor polymer.[25]

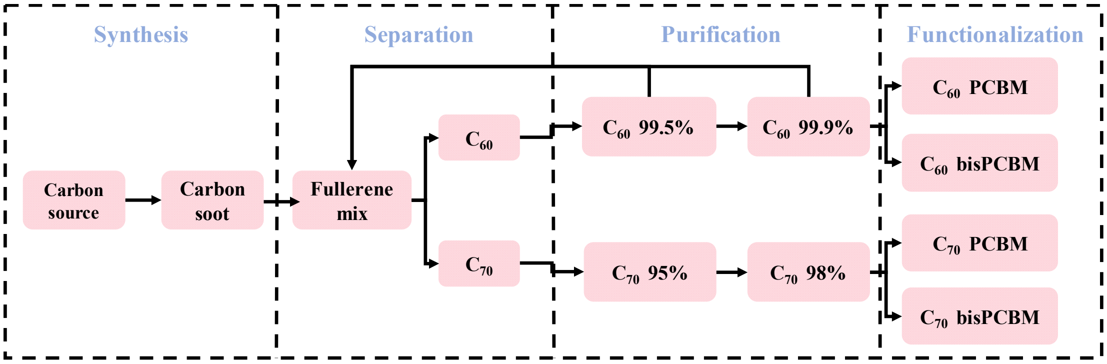

***Figure 2.5**. Overview of the process flow to produce modified fullerene compounds (reproduced from ref. 54).*

2.3.2 Pristine vs. substituted fullerenes

A number of neat fullerenes exist but for most applications only the fullerenes C_{60} and C_{70} are of interest. Both can be easily obtained in large quantities. However, their low solubility in organic solvents and their strong tendency to crystallize complicates processing with common coating and printing technologies.[56,57] Both, C_{60} and C_{70} show a bell shaped solubility behavior (where solubility peaks at a certain temperature) with a maximum solubility of about 27 g L^{-1} at 37 ˚C for C_{60} and 38 g L^{-1} at 55 ˚C for C_{70} in o-DCB (see **Figure 2.6**).[58,59]

The first study that used fullerenes as an acceptor material was reported in 1995 by Yu *et al*., who studied a BHJ blend of the polymer MEH-PPV with C_{60} and its functionalized derivatives ([5,6]-PCBM and [6,6]-PCBM).[47] PCBMs are a preferred acceptor material due to the higher solubility, and the absence of crystallization during film formation.

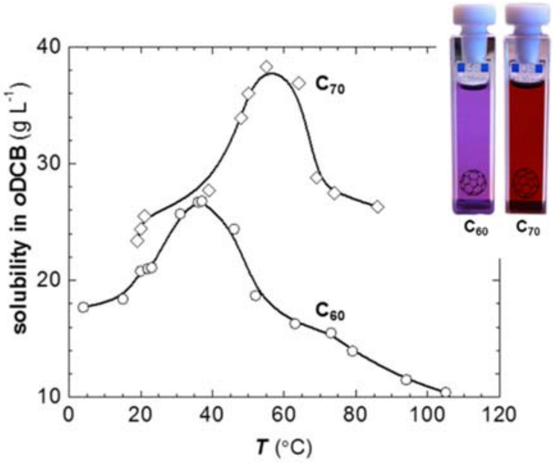

***Figure 2.6** Solubility of C_{60} (circles) and C_{70} (diamonds) in o-DCB as function of temperature. (adapted from Paper I)*

During derivatization, chemical reactions take place on one of the double bonds of the fullerene. In C_{60}, all the conjugated bonds are equal, which means that in most reactions a single reaction product is formed. Reactions on C_{70} lead to the formation of a mixture of structural isomers because the 35 double bonds in C_{70} are not all equal due to the lower symmetry of the fullerene cage.[42]

Table 1. *Embodied energy and current cost to purchase 1 g of various fullerenes [source Solenne BV and ref.54].* ***1 € = 1.1 $**

Fullerene	**cost** (€ g^{-1})	**Embodied energy** (GJ kg^{-1})
C_{60}	*15*	*25*
C_{70}	*150*	*38*
$PC_{61}BM$	*150*	*65*
$PC_{71}BM$	*780*	*90*

One disadvantage of using fullerene derivatives is the high embodied energy needed for production (see **Figure 2.7**). The as-synthesized C_{60}:C_{70} mixture entails only about 8 GJ kg^{-1} of embodied energy, which increases to 25 GJ kg^{-1} for C_{60} and 38 GJ kg^{-1} for C_{70} after separation and purification. Instead, fullerene derivatives *i.e.* $PC_{61}BM$ and $PC_{71}BM$ consume as much as 65 and 90 GJ kg^{-1}, respectively (**Table 1**). A higher embodied energy leads to an increase in material cost,[54] which is associated with the additional synthesis step for further functionalization. As result, $PC_{61}BM$ and $PC_{71}BM$ are considerably more expensive materials compared with the neat fullerenes (see **Table 1**). Hence, selection of the electron acceptor material requires a compromise between solubility and material cost. This thesis demonstrates that a mixture of C_{60}:C_{70} can be successfully employed in organic optoelectronic devices, thereby reducing both the embodied energy and, ultimately, cost.

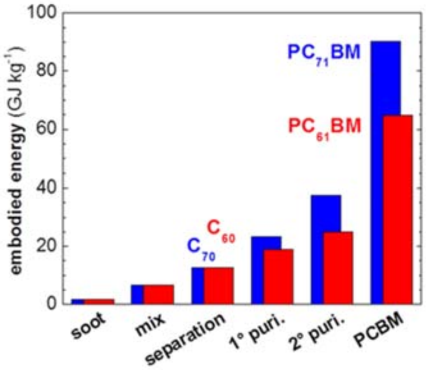

Figure 2.7 *Embodied energy for C_{60} and C_{70} products as a function of production stage. (reproduced from ref.54)*

2.4 Photovoltaic device operation

2.4.1 Organic bulk-heterojunction

The first observation of photoconductivity in solid anthracene was reported in 1965.[60] In the 1980s, polymers such as poly(sulphur nitride) and polyacetylene were used for the first time as a single layer in photovoltaic cells.[17] However, this type of architecture limited PCEs to values below 0.1%. Due to the low dielectric constant of organic semiconductors, the possibility of forming free charge carriers upon light absorption is low.

In 1986, Tang reported a two-layer organic photovoltaic device, bringing together an electron donor material (phthalocyanine dye) and an electron acceptor material (perylene tetracarboxylic derivative) in a bilayer cell to dissociate excitons, resulting in a PCE of 1%, which marks the starting point for modern organic photovoltaics.[61] One challenge with this kind of architecture is that the exciton diffusion length in organic materials is typically 1-10 nm.[62] Therefore, excitons must be generated in close proximity to the donor:acceptor interface where dissociation can take place. As result, only material within a few nanometers of the bilayer interface generates photo-induced charges.

To overcome this problem, Heeger and Friend independently introduced the so-called bulk heterojunction (BHJ) architecture (see **Figure 2.8c**), which consists of two finely intermixed materials (electron donor and acceptor) deposited as a thin film. The BHJ contains a large number of donor:acceptor interfaces distributed throughout the bulk of the active layer.

The work on BHJs was enabled by the discovery of fullerenes in 1985, for which the Nobel prize in Chemistry was awarded to Robert F. Curl., Harold W. Kroto and Richard E. Smalley.[41] Due to their high electron mobility, and arguably, symmetry, fullerenes are the most widely used electron acceptors in bulk-heterojunction devices.

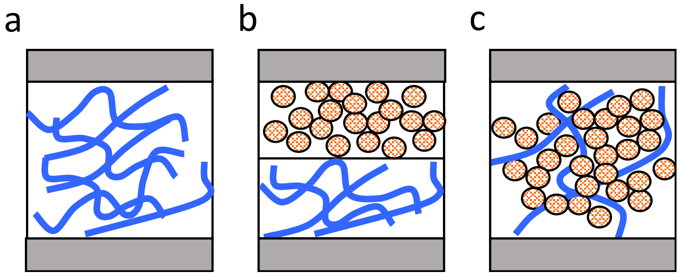

***Figure 2.8** Schematics of different solar cell architectures: a) single layer, b) bilayer and c) bulk heterojunction.*

The resulting film of inter-mixed donor and acceptor materials is said to form an interpenetrating network of the donor and acceptor material. Initial attempts to describe the nanostructure of BHJs only considered pure domains of the donor and acceptor (**Figure 2.9**).[47] Although this picture is useful for conceptual understanding, it is now established that many donor:acceptor blends give rise to a mixed phase. Co-existence of a mixed and a pure phase, creates an energy cascade which aids charge separation and therefore improves the free charge carrier collection efficiency.[63]

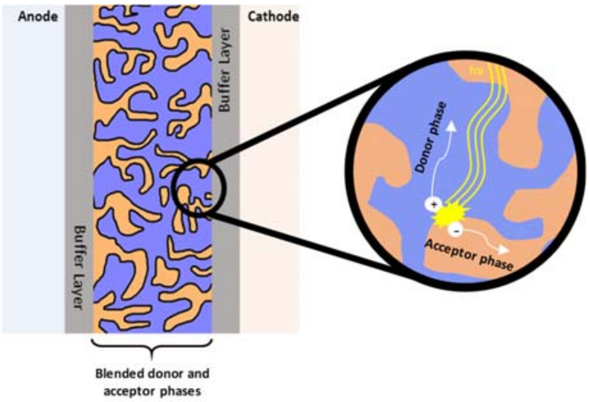

Figure 2.9 *Schematic of a BHJ with acceptor rich (blue) and donor rich (orange) phases. Note that neither phase is necessarily pure but may dissolve a certain amount of the second (donor or acceptor) moiety.*

From a thermodynamic point of view, it is important to consider the miscibility of the individual components to identify the different phases upon solidification. **Figure 2.10** represents the schematic of the different nanostructures that can be encountered when two components (D:A) are blended together. Immiscible components can form a largely separated binary system of pure phases of each component. This is not desirable due to the limited exciton diffusion length and the limited amount of donor:acceptor interface. On the other hand, completely miscible components lead to a one phase system but may also promote recombination (due to the large number of charge transfer (CT) states) and hinder charge transport. Most likely, the best-case scenario is where a two or three phase system is encountered (intermixed regions and pure phases of the components), offering the advantages of both, phase purity and miscibility. Although the discussion with regard to pure versus mixed phases is ongoing, it is generally assumed that at least three phases (intermixed regions co-exist alongside relatively phase-pure domains of the individual components) exist in most high-performance organic solar cells.[64,65]

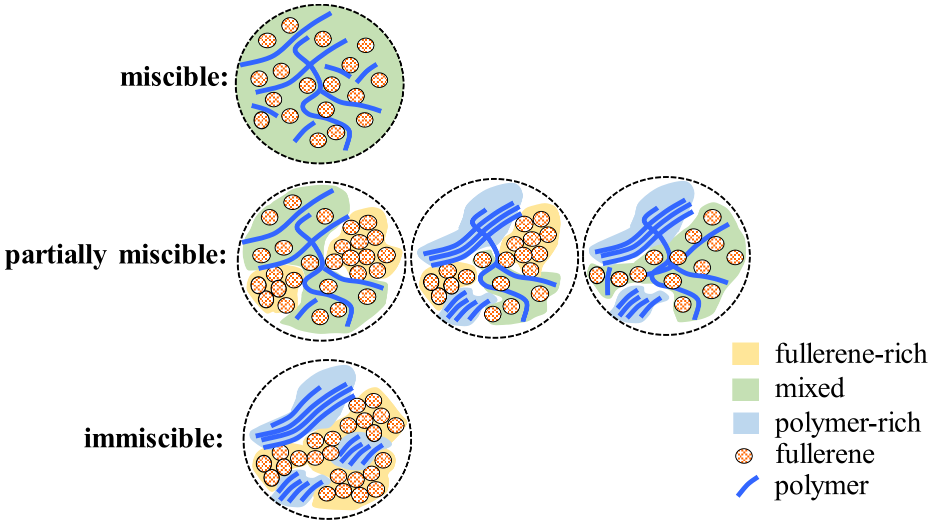

Figure 2.10 *Schematics of the different nanostructures that can be encountered for a two component system (D:A).*

Nanostructure formation in BHJ blends depends on: (i) the chemical structure of the donor and acceptor materials and (ii) the processing conditions during device fabrication, which strongly influence the solidification kinetics. The former impacts the solubility, miscibility with other components, photochemical stability, *etc*. Processing parameters such as the choice of solvent,[66] the use of processing additives[67] or annealing,[32,68] can also affect the nanostructure (e.g. the degree of order, phase separation, and presence of finely intermixed phases). For instance, even a D:A combination that is thermodynamically immiscible in the solid state, can lead to a (kinetically trapped) one phase nanostructure if the mixture solidifies sufficiently rapidly from a homogeneous solution. One emerging tool that permits to gain additional control over the solidification kinetics is the use of ternary blends. This approach will be further explored in Chapters 4 to 6.

2.4.2 OPV device architectures

In OPV devices, the active layer is sandwiched between two electrodes. Typically, a transparent semiconducting substrate (patterned indium tin oxide (ITO) on glass as in paper I, II and IV) is used as one of the electrodes, whereas the other electrode is typically a metal (in paper I, II and IV aluminium was used due to low cost and ease of evaporation; see **Figure 2.11**). Different interlayers are introduced to adjust the work function of the electrodes between the active layer and the electrodes (in paper I, II and IV a thin layer of water dispersed poly(3,4-ethylenedioxythiophene): poly(styrenesulfonate) (PEDOT:PSS) and lithium fluoride (LiF) were used as interlayers).

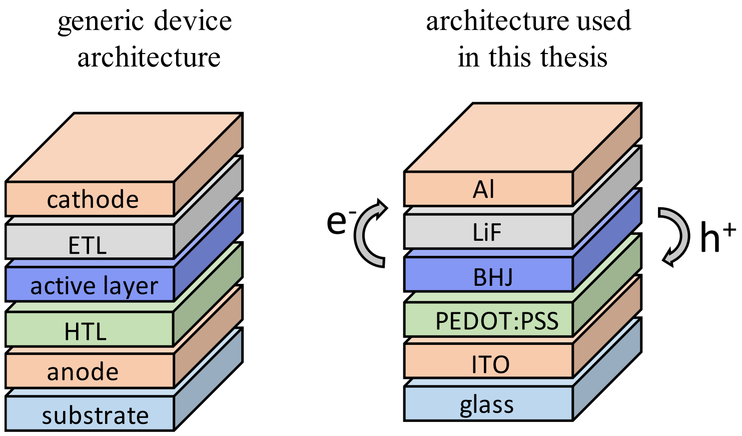

Figure 2.11 *Schematic of a standard structure for single-junction organic bulk-heterojunction solar cells with the respective electrodes (cathode and anode) and interlayers (electrons transfer layer ETL and holes transfer layer HTL).*

More recently, alternative approaches are being explored, including tandem and ternary OPVs, which have enabled breakthrough efficiencies of 11%.[69] This will be discussed in more detail in the following chapters.

2.4.3 Working principle

The phenomenon of converting light into electric current within an organic solar cell can be divided into six different steps (see **Figure 2.9 and 2.12**): (a) upon absorption of a photon by the active layer (mostly the donor material as in paper I, II and IV), an electron is photoexcited from the HOMO to the LUMO, leading to the formation of a tightly bound electron-hole pair, or so-called exciton. (b) The exciton can diffuse towards the donor:acceptor interface, then (c) the exciton dissociates first into a weakly bound charge-transfer state at the interface, and (d) finally into free charge carriers. The exciton diffusion length in organic semiconductors before recombination occurs is typically 1-10 nm,[62] which means that the donor:acceptor interface should ideally be very close to the molecule where the photo-excitation occurs. (e) The free charge carriers then drift toward the electrodes, driven by the built-in bias, originating from the different work functions of the electrodes. (f) Photo-generated holes and electrons are extracted at the respective electrodes generating an electrical current.

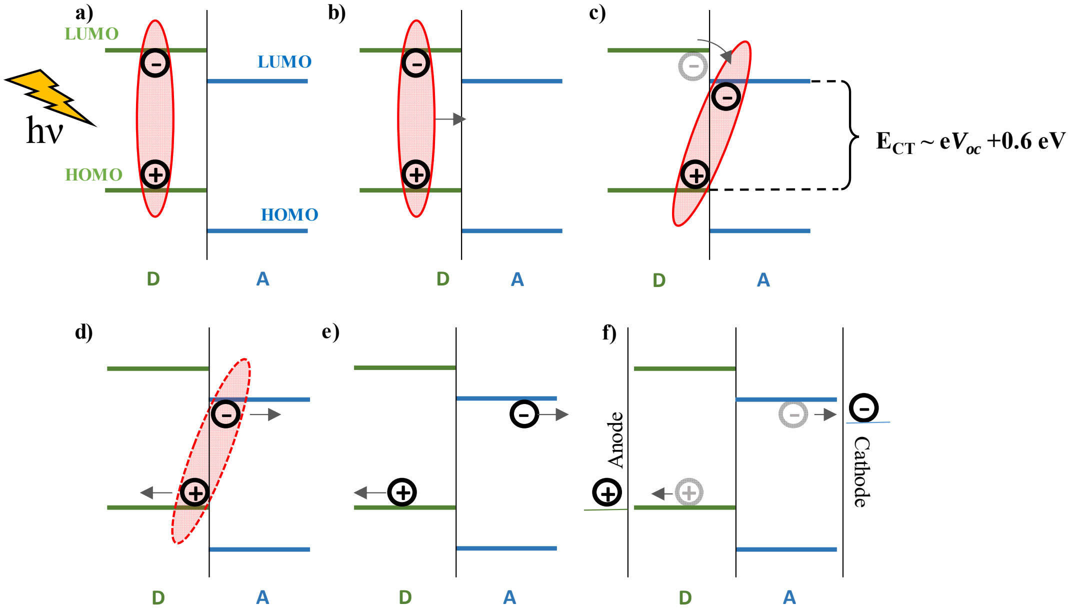

Figure 2.12 *Illustration of the working principle of charge generation in a donor:acceptor bulk heterojunction solar cell.*

The driving force for exciton separation in the bulk-heterojunction is the result of the difference between the respective donor and acceptor LUMO levels, which normally is required to be ~ 0.2-0.3 eV (cf. **Fig. 2.12c**). However, some BHJs with no driving force have been reported, such as, for instance blends of low band-gap isoindigo polymers and fullerenes.[70]

The LUMO of the acceptor and the HOMO of the donor are particularly important, as they define the maximum attainable energy for a given D:A combination. The $\text{HOMO}_{\text{donor}}$ - $\text{LUMO}_{\text{acceptor}}$ difference is referred to as the energy of the charge transfer state and defines the open-circuit voltage: $E_{CT} \sim e\,V_{oc} + 0.6\ eV$.[71]

2.4.4 Photovoltaic characteristics

To evaluate (organic) solar cells the power output is normally measured under a solar simulator lamp with a standardized AM1.5 solar irradiance spectrum. Under that condition, one sun is defined as equal to 100 mW/cm^2 of irradiance and it corresponds to the intensity of the sunlight during a cloudless day. Once the light is absorbed by the cell, a photocurrent is recorded and normalized with respect to the device area. Upon plotting the photocurrent density versus voltage, the IV-curve is produced (see **Figure 2.13**). Different parameters can be extracted from the IV-curve for further evaluation of the device.

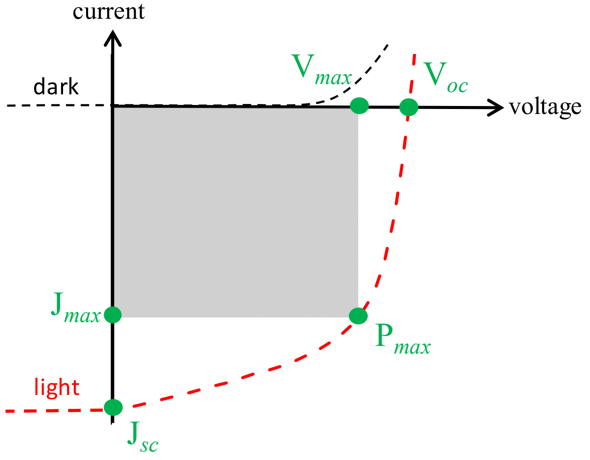

Figure 2.13 *Schematic of current density-voltage (IV) curve of a photovoltaic cell under illumination (red dashed line) and in the dark (black dashed line).*

The *short-circuit current density* (J_{sc}) is the photocurrent that the photovoltaic device generates at short circuit, giving information about the charge separation and transport efficiency within the cell. It can be quantified by directly connecting the two electrodes, and illuminating the cell. There are different loss mechanisms that can limit the J_{sc} such as incomplete light absorption, poor charge generation and transport.

The *open circuit voltage* (V_{oc}) is determined by the difference in the HOMO level of the donor and the LUMO level of the acceptor, typically around V_{oc} ~ 0.5-1.2 V for polymer:fullerene blends.[63,71] It can also be directly related to the energy of the *CT-state*.[72]

The *fill factor* (*FF*) is calculated by the ratio between the maximum power point (*MPP*) and the product of J_{sc} and V_{oc}:

$$FF = \frac{P_{max}}{J_{sc} \times V_{oc}} \tag{eq.1}$$

The *power conversion efficiency* (*PCE*) or the *MPP* is defined as the ratio of the electric power (P_{max}) that is generated, and the power of the incident light P_{in}. The PCE is characterized by three parameters: J_{sc}, V_{oc} and *FF*:

$$PCE = \frac{P_{max}}{P_{in}} = \frac{FF \times J_{sc} \times V_{oc}}{P_{in}} \tag{eq. 2}$$

Another way to evaluate the photovoltaic performance is to measure the EQE. The EQE measures the ratio between the number of charge carriers collected by the solar cell and the incident photons as a function of their energy.

2.5 Life time and stability of OPVs

The stability is one of the most critical aspects from a commercialization perspective. The lifetime of OPVs can be limited by different factors over the service of the module. For instance, water, oxygen, irradiation, and heating are some of the main factors that limit the stability of a solar cell. Those factors directly affect the nanostructure of the active layer, the decay of electrode materials and buffer layers and introduce mechanical stress between these layers. Thermal stability is here discussed in terms of changes in nanostructure. Thermal degradation, which is only pronounced if organic semiconductors are heated under illumination and in contact with air, is not considered. In terms of thermal stability of the nanostructure of the active layer BHJ several strategies have been advanced and some of them are summarized below:

- *material design:* strategies like the use of cross-linkable side chains,[73–75] rigidity/flexibility of polymer chains,[24] high T_g materials,[24] decreased fullerene crystallinity or glass formation,[76] improve the thermal stability.

- *Processing methods:* No use of high boiling point solvents, which can get trapped in the deposited films and increase the molecular mobility of $PC_{61}BM$ within the polymer matrix and promote the growth of large $PC_{61}BM$ crystals.[77] Illumination of the active layer induces the oligomerization of $PC_{61}BM$, which can suppress aggregation and crystallization of $PC_{61}BM$.[78]

- *Device engineering within the active layer:* adding a third light absorbing component to the blend can vitrify the nanostructure, which improves the thermal stability.[79,80]

The aim of this thesis is to use ternary blends based on fullerene mixtures to produce thermally stable organic solar cells, the discussion is then expanded to fullerene-free ternary blends. The use of molecular glasses as a tool to control the nanostructure of ternary BHJ is highlighted in chapter 3, 4, 5 and 6.

3

3 Glass formation by organic semiconductors and blends

Solution processing of organic semiconductors is a principal paradigm of organic electronics. Coating and printing techniques are thought to enable the cost-effective manufacture of large-area devices, such as electronic circuitry and solar cells, ideally on flexible substrates. Solidification of an organic semiconductor occurs through removal (evaporation) of the processing solvent, which should occur *rapidly* to facilitate high-throughput printing. The resulting solid-state nanostructure tends to be located far away from thermal equilibrium because the individual components of the semiconductor material did not have sufficient time to fully crystallize or adopt a relaxed conformation in case of disordered phases.

A prime example is solution-casting of the widely studied donor:acceptor binary P3HT:PCBM, which initially results in a largely disordered material. Thermal annealing of P3HT:PCBM solar cells is critical for optimizing their photovoltaic performance, which results in crystallization of the blend components.[32,81] Crystallization of in particular the polymer occurs above 50 °C, which corresponds to the glass transition temperature T_g of the initially homogeneous blend.[24,82] Hence, the T_g represents a critical parameter that indicates the minimum temperature required for thermal annealing.

Another typical system, which will be discussed further in this thesis, is represented by a blend of the thiophene-quinoxaline copolymer TQ1 (see **Figure 2.3** chapter 2) and $PC_{61}BM$. Solar cells based on an as-cast active layer of TQ1 and $PC_{61}BM$ display a PCE of about 4%, which however decreases as soon as the T_g of the blend is reached.[83] Since TQ1 does not feature a crystalline phase,[84] the TQ1:$PC_{61}BM$ blend undergoes phase-separation through liquid-liquid demixing, which has a detrimental effect on the photovoltaic performance. In addition, the fullerene material forms micrometer sized crystals. Evidently, for blends based on non-crystalline donor polymers the T_g represents the upper limit for thermal stability.

Detailed knowledge about the glass transition of organic semiconductor blends is therefore critical for both the selection of optimal processing schemes (e.g. thermal annealing), as well as the thermal stability of the nanostructure during processing and operation (cf. Chapter 6). This chapter discusses the solidification kinetics and vitrification (glass formation) of one- as well as multi-component systems. Two techniques are introduced that are used in this thesis to determine the glass transition temperature: differential scanning calorimetry (DSC) and plasmonic nanospectroscopy.

3.1 Origin and kinetic aspects of the glass transition

Any chemical system attempts to reach thermodynamic equilibrium, which changes with temperature and pressure. "*If a system is disturbed from its state of equilibrium it relaxes to that state, and the process is referred to as relaxation.*" (IUPAC Gold Book on *relaxation*) In case of macromolecules, relaxation requires reorganization of the polymer chain through translational and, in particular, rotational motion. These relaxation processes are thermally activated, and therefore occur more frequently the higher the temperature. There exists a temperature, the so-called glass transition temperature T_g, where the time needed for relaxation becomes comparable to the experimentally available timescale. For instance, the duration of a thermal annealing experiment at a temperature T_{anneal} represents the time that is available for relaxation to occur at this particular temperature. The further the polymer is cooled below T_g, the more time is required for relaxation. Ultimately the existing chain conformation is said to be *frozen in,* since relaxation will only occur very slowly. Here, it should be noted that relaxation nevertheless occurs over a sufficiently long period of time, which in practice may far exceed the *shelf life* of a polymer.

The glass transition of a polymeric material can be intuitively understood when considering the viscoelastic response at different temperatures. Consider a periodic (sinusoidal) deformation experiment with a low strain amplitude, which is carried out at different temperatures. The inverse of the rate of deformation is proportional to the experimental timescale that is available for relaxation. Far below the T_g, where main chain relaxation only occurs at an exceedingly long timescale, the polymer is said to be *glassy*. The material displays a high elastic modulus, and would fail in a brittle manner if the strain was increased further. Instead, sufficiently above T_g, the polymer is *rubbery* (provided the polymer is entangled), i.e. the material displays a much lower elastic modulus, since now the main chain is able to rapidly adopt a more extended conformation to accommodate the additional strain. Here, it should be noted that the glass transition temperature depends on the deformation rate: the more rapidly a polymer is deformed the shorter the timescale that is available for relaxation and, hence, the higher the T_g.

The time required for main chain relaxation τ_α is given by the empirical Vogel-Fulcher-Tamann (VFT) equation, which holds for amorphous polymers in the temperature range $T_g < T < 100$ °C:

$$\tau_\alpha(T) = \tau_0 \cdot exp\left(\frac{B}{T - T_0}\right) \qquad \text{(eq. 3)}$$

where τ_0, B and T_0 are constants. Hence, the relaxation time exponentially increases as the temperature is lowered. For instance, the constants reported for the polyfluorene F2/6 in Ref. 85 correspond to a value of, e.g., $\tau \sim 1$ s at 70 °C and $\tau \sim 100$ s at 56 °C. The *operational* glass transition temperature T_g, which is often quoted as a fixed parameter but should be considered as rate-dependent, is commonly defined as the temperature for which $\tau_\alpha = 100$ s (i.e. $T_g = 56$ °C for F2/6). The T_g values reported in this thesis were measured at a rate of 5 or 10 °C min^{-1}, which is a range that is typically found to correspond to a relaxation time of about 100 s.

3.2 Measurement of the glass transition temperature

A number of experimental techniques can be used to measure the glass transition temperature. The most advanced techniques such as dynamic mechanical analysis (DMA), rheology and broadband dielectric spectroscopy (BDS) provide information about the rate-dependence of the T_g, but tend to require too much material to be readily applicable to organic semiconductors. Here, it is interesting to note that two recent reports demonstrate highly reliable DMA and rheology measurements of a range of conjugated polymers with only 10-20 mg of material.[86,87] DSC, for which the rate is more limited unless more specialized rapid heat/cool calorimeters are used, is the most readily accessible technique but in case of many conjugated polymers such as TQ1 and PTB7 fails to reveal the T_g. Here, a recent theoretical study by Root et al. is interesting to consider, which used molecular dynamics simulations to predict the glass transition temperature of these two polymers to be $T_g \sim 102$ °C and 127 °C, respectively.[88]

Techniques that permit to study the thermal behavior of thin films of organic semiconductors are of high interest since the results are directly applicable to the active layer thickness of organic electronic devices. This is because the thermal behavior of thin films can strongly deviate from that of the bulk because of interface and/or confinement effects. Variable-temperature ellipsometry has been most widely explored for this purpose,[24,89,90] and in case of TQ1 yields a value of $T_g \sim 100$ °C.[91] Ellipsometry allows to extract the change in film thickness *d* with temperature, and therefore can be used similar to classical dilatometry to detect phase transitions. The glass transition is a second order phase transition, meaning that variables such as the volume *V* change continuously, whereas the first derivative, i.e. the thermal expansion coefficient α, shows a step change (**Figure 3.1**):

$$\alpha = \frac{1}{V}\left(\frac{dV}{dT}\right)_p \qquad \text{(eq. 4)}$$

In case of ellipsometry the film thickness and volume are considered to be proportional, $d \propto V$.

In this thesis, DSC is correlated with a for organic semiconductors new technique, plasmonic nanospectroscopy, which is a highly attractive technique due to its exceptional sensitivity to small changes in refractive index, as discussed below.

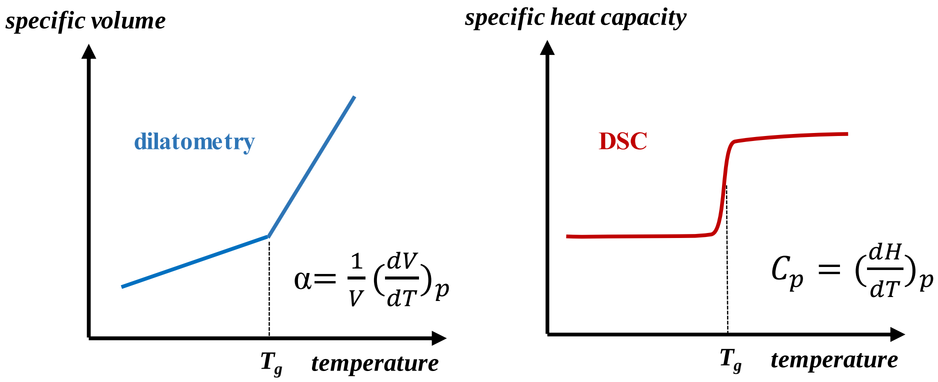

Figure 3.1 *Illustration of the glass transition temperature measurement by dilatometry and DSC.*

3.2.1 Differential scanning calorimetry (DSC)

DSC records the difference in heat flow to/from a sample during heating/cooling as compared to a reference, and thus allows to monitor the additional heat required or released by the sample during melting or crystallization. The glass transition manifests itself as a *step change* in the heat capacity C_p (**Figure 3.1**), i.e. the heat required to increase the temperature of the sample by a certain degree:

$$C_p = \left(\frac{dH}{dT}\right)_p \qquad \text{(eq. 5)}$$

where H is the enthalpy. For some materials such as rigid rod conjugated polymers the step change in heat capacity is minute, possibly because of the presence of local order, and thus can only be observed with great difficulty.

3.2.2 Plasmonic nanospectroscopy

In this thesis *plasmonic nanosprectroscopy* is utilized as a technique to monitor thermal transitions in thin films of conjugated polymers. The same technique has been used previously by Langhammer et al. to measure the size-dependent glass transition temperature of polystyrene (PS) nanoparticles and poly(methyl methacrylate) (PMMA) thin films.[92] The fabrication of the sensor platform and all measurements were carried out by Ferry Nugroho at the Department of Applied Physics of Chalmers University of Technology. The sensor platform consists of quasi-random arrays of silver or gold disks (radius = 170 nm; height = 20 nm. silver in Paper III, gold in paper IV) on a glass substrate and coated with a 10 nm thin silicon nitride support layer (**Figure 3.2**). The nano-disks sustain *localized surface plasmon resonance* (LSPR), which gives rise to a locally enhanced electric field that depends on the refractive index of the local environment surrounding them. When covered with a polymer film the position of the LSPR extinction peak is thus sensitive to the precise refractive index of the polymer. By following the optical readout one is able to monitor any changes occurring in the polymer. Heating of the polymer film gives rise to thermal expansion and hence an increase in film thickness (cf. eq. 4), which decreases the density and hence refractive index. As a result, the position of the LSPR extinction peak $\Delta\lambda_{peak} = \lambda_{peak}(T) - \lambda_{peak}(RT)$ changes with temperature, where $\lambda_{peak}(T)$ and $\lambda_{peak}(RT)$ are the peak wavelength at temperature T and room temperature, respectively. A change in slope of the LSPR extinction peak, $d(\Delta\lambda_{peak})/dT$, indicates that the material undergoes a phase transition, and can be used to detect for instance the T_g of different conjugated polymers. The technique is described in more detail in Paper III and IV.

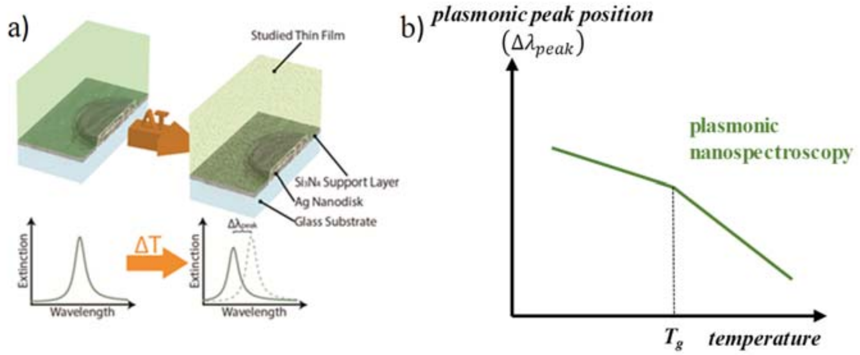

Figure 3.2 *a) Schematic of the operation principle of plasmonic nanospectroscopy. (adapted from Paper III). b) Schematic of* T_g *measurement with plasmonic nanospectroscopy.*

Since plasmonic nanospectroscopy is a new technique, a range of samples from amorphous PMMA, to liquid-crystalline APFO3 and F8BT, semi-crystalline P3HT and a P3HT:PCBM blend were compared with DSC measurements (**Table 2**). Results for polymer:fullerene alloy ternary blends are discussed in Chapter 5. For each material but P3HT the glass transition could be readily detected with plasmonic nanospectroscopy as a distinct change in slope of $\Delta\lambda_{peak}(T)$. Generally, the two techniques are in good agreement. In case of F8BT and APFO3 the obtained T_g is higher when measured with either DSC or plasmonic nanospectrosocopy, respectively. This observation underlines that thermal transitions of thin films and bulk materials can deviate from each other. For the materials based on TQ1 the $T_g \sim 113$ °C could only be detected with plasmonic nanospectroscopy, which is similar to values obtained with ellipsometry and molecular dynamics simulations.[91,93] Interestingly, in case of melting transitions only a temperature range can be identified, which corresponds to the onset and endset measured with DSC, and not the peak melting temperature.

Table 2. Thermal Transition Temperatures Measured with Plasmonic Nanospectroscopy and DSC[a]. [a]Glass transition temperature, T_g (inflection point for DSC); melting temperature, T_m (onset/endset for plasmonic nanospectroscopy and peak value for DSC); nematic to isotropic transition temperature, T_{lc} (peak value for DSC); n.m. = not measured. [b]Same APFO3 batch and DSC measurement as in ref.[24]. [c]Extrapolated bulk values. [d]Value from ref.[84]. [e]T_m (cf. ref.[94]). [f]Same F8BT batch and DSC measurement as in ref.[95]. Table reproduced from Paper III.

	polymer structure	T_g (°C)		T_m (°C)		T_{lc} (°C)	
		plasmonic nanospectroscopy	DSC	plasmonic nanospectroscopy	DSC	plasmonic nanospectroscopy	DSC
PMMA	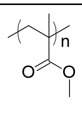	108	124	-	-	-	-
F8BT[f]	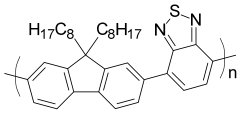	109	120	199-226	223	259	270
APFO3[b]	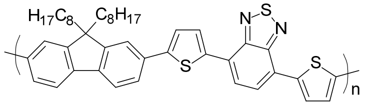	124	109	-	-	n.m.	197
TQ1	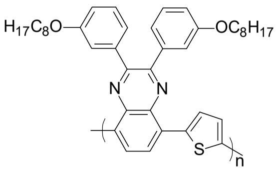	113^c	n.m.	-	-	n.m.	300^d
2:1:1 TQ1:$PC_{61}BM$: $PC_{71}BM$		120^c	n.m.	-	-	-	-
P3HT	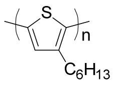	n.m.	n.m.	190-235	235	-	-
1:1 P3HT: $PC_{61}BM$		74	60	166-205	198^e	-	-

3.3 Crystallization kinetics and vitrification

This section will explain why mixing of several components can reduce the rate of crystallization and hence increases the tendency for glass formation, provided that the resulting miscible liquid is cooled sufficiently fast.

The rate of crystallization is determined by two processes, nucleation and growth. Classical nucleation theory describes the rate of homogeneous nucleation of a single-component system according to: [96]

$$\text{rate of nucleation} \propto D(T) \cdot exp\left(-\frac{\Delta G^*}{kT}\right) \tag{eq. 6}$$

Where $D(T)$ is the diffusion coefficient and ΔG^* is the change in Gibbs free energy upon formation of a critical nucleus. The diffusion coefficient D describes the ability of molecules to diffuse towards the growing crystal and, according to the Stokes-Einstein relation, is inversely related to the viscosity η, which is proportional to the relaxation rate as given by the VFT equation (cf. eq. 3). The free energy needed for nucleation represents an energy barrier and is given by:

$$\Delta G^* \propto 1/\Delta G_c^2 \tag{eq.7}$$

where ΔG_c is the difference in free energy between the crystalline and liquid (glassy) state. The free energy of crystallization can be related to the undercooling below the melting temperature T_m:

$$\Delta G_c = \Delta H_m \cdot \frac{\Delta T}{T_m} \tag{eq.8}$$

where $\Delta T = T_m - T$ is the degree of undercooling.

The rate of crystal growth can be expressed as: [96]

$$\text{rate of growth} \propto D(T) \cdot \left[1 - exp\left(-\frac{\Delta G_c}{kT}\right)\right] \tag{eq. 9}$$

Both the rate of nucleation and growth have a kinetic component, the diffusion term, which increases exponentially above the glass transition temperature T_g according to the VFT equation (cf. eq. 3), as well as a thermodynamic component, which increases with the degree of undercooling below T_m. The rate of nucleation and growth typically peak close to T_g and T_m, respectively (**Figure 3.3a**). Overall, crystallization can only occur if both nucleation and growth occur at a final rate. Therefore, the rate of crystallization peaks at an intermediate temperature between T_g and T_m.

Information about the rate of crystallization can be used to construct so-called time-temperature-transformation (TTT) diagrams, which provide insight into the degree of crystallization that will be reached through a particular choice of solidification protocol, as well as the likely prominence of either nucleation or growth (**Figure 3.3b**). Moreover, the rate of solidification can be estimated that is needed to quench the material to a glassy state where no, or very few crystalline domains are present. Also, it is evident that a reduction in the rate of crystallization (equivalent to a shift of the isenthalpic lines to the right in **Figure 3.3b**) will result in a material that is more likely to form a glass.

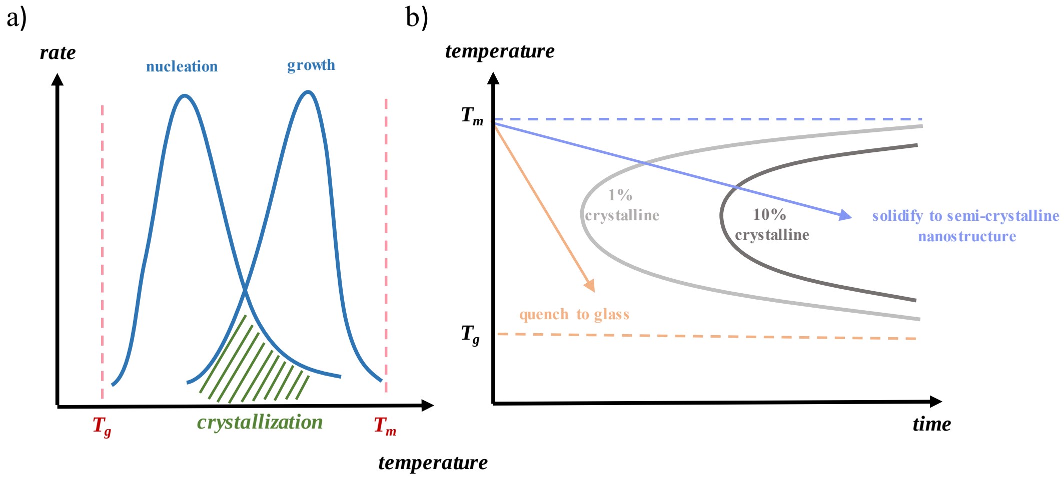

Figure 3.3 *a) Schematic of rate of nucleation and growth b) Schematic of a time-temperature-transformation (TTT) diagram. The red and blue lines represent a constant cooling rate that leads to glass formation and a semi-crystalline solid, respectively.*

The crystallization rate of a multi-component system is –just like that of a single-component system– determined by the rate of nucleation and growth. If the components are miscible then mixing decreases the free energy of the liquid relative to that of the individual components.

For an ideal solution where the enthalpy of mixing $\Delta H_{mix} = 0$, the free energy change of mixing $\Delta G_{mix} = \Delta H_{mix} - T\Delta S_{mix}$ of n components only depends on the entropy of mixing:

$$\Delta S_{mix} = -Nk_B \sum_{i=1}^{n} \phi_i \ln \phi_i \qquad \text{(eq. 10)}$$

where ϕ_i is the volume fraction of component i, and N is the total number of molecules. For a non-ideal solution, the free energy of mixing can decrease even more if $\Delta H_{mix} < 0$, which can arise due attractive molecular interactions such as π-stacking or hydrogen bonding between the components.

For an ideal solution, the highest entropy of mixing is obtained if the volume fraction of each component is equivalent. The same concept is prevalent in the field of *high entropy alloys*, where typically five or more components are mixed at a (close to) equimolar ratio.[97] Chapter 4 will discuss how the increase in the entropy of a mixture of molecules (C_{60} and C_{70}) gives rise to a higher solubility in a common solvent, which reaches a maximum at a 1:1 stoichiometry.

Since the free energy of an ideal multi-component liquid is lower than the sum of the free energies of the single-component liquids by $\Delta G_{mix} = -T\Delta S_{mix}$, the difference in the free energy change of crystallization ΔG_c is likewise reduced.[98] Inspection of equations 6 and 9 indicates that a lower ΔG_c decreases both the nucleation and growth rate. It can be concluded that mixing of two or more components reduces the overall crystallization rate, which increases the likelihood for glass formation. The highest tendency for glass formation of an ideal multi-component system should occur for a 1:1 stoichiometry, where also the highest solubility in a common solvent can be expected.

Here it is interesting to note that the concept of multi-component mixtures is widespread in the field of pharmacy, where *amorphous drugs* are preferred because of their higher rate of dissolution.[99] Likewise, in metallurgy the field of *metallic glasses* utilizes mixtures of different elements to influence the rate of crystallization.[100]

4

4 Organic solar cells based on neat fullerene alloys

Ternary blends permit to achieve both, high solar cell efficiencies and a high degree of thermal stability. For $PC_{61}BM$:$PC_{71}BM$ based devices a performance of up to PCE ~11% has been reported, which is comparable to the highest values reached with binary and/or tandem solar cells.[69]

Generally, the active layer of ternary solar cells consist of three components, the predominant donor:acceptor (D:A) system and a third component, which can be a polymer, small molecule, a dye or a nanoparticle.[101–103] Ternary organic solar cells can be classified into three categories:

- two donors and one acceptor (D_1:D_2:A).[104–107]
- one donor and two acceptors (D:A_1:A_2).[79,108–111]
- one donor, one nonvolatile additive and one acceptor (D:NA:A).[112–115]

The use of three-component mixtures can result in different types of phase behavior, which strongly influences how the V_{oc} evolves with composition. There are two main types of ternary systems: (i) binary or pseudo-binary systems that results from *alloy* formation of synergistic components, and (ii) true ternary systems, which arise as a result of the *immiscibility* of the three components.[76,116,117] For the former type of system, Street *et al.* reported for a D_1:D_2:A and D:A_1:A_2 systems that the V_{oc} displays a linear dependence with the amount of the third component, which allows to tune the device performance.[118] Instead, for phase-separated ternaries, which feature no alloy formation, the resulting V_{oc} corresponds to the low-V_{oc} binary.[119]

This chapter discusses the solubility and solution processing of neat fullerenes and neat fullerene mixtures, which are used as an acceptor material for organic photovoltaics. The use of ternary blends as a more cost-effective yet efficient alternative is introduced. This chapter will focus on the second ternary solar cell category (D/A_1/A_2) and the results presented in paper I and paper II, where different donor polymers have been used to explore this strategy.

4.1 Solubility and processing of pristine fullerenes and fullerene mixtures

The solubility of polymer and small molecule semiconductors is a prerequisite for solution-processed organic photovoltaics, influencing processability and solid state nanostructure formation, which in turn affects the opto-electronic behavior.[120] Prior to evaporation of the processing solvent, the solubility of the different compounds within the solvent determines the onset of phase separation and the presence of aggregates that form at a given temperature and concentration. Therefore, control of the solubility can be regarded as a tool to guide formation of the bulk-heterojunction nanostructure.

The most common strategy to enhance the solubility of organic semiconductors in organic solvents is the decoration with flexible pendant groups (side chains in case of polymers) that reduce the tendency for π-stacking and increase the entropy of the solubilized state. For instance, highly soluble fullerene derivatives such as PCBMs carry butyric acid methyl ester groups. Ideally, the amount of solubilizing pendant groups is minimized since they introduce defects and energetic disorder that can negatively affect charge transport. However, they are necessary to enable solution processing, which can result in a trade-off for organic photovoltaics.

With the aim to establish a route towards high-performance and cost-effective organic solar cells, two materials systems were explored based on polymer:fullerene D/A_1/A_2 ternary blends. Neat fullerene mixtures of C_{60} and C_{70} were used as an electron acceptor material. The motivation for using neat fullerenes instead of fullerene derivatives such as $PC_{61}BM$ and $PC_{71}BM$ is the reduced cost of the material (see **Table 1** in chapter 2), as well as their tendency to vitrify upon mixing, as discussed in this chapter.

C_{60} appears purple in solution whereas C_{70} displays a more ruby-like color due to the stronger absorption in the 400-600 nm range (**Figure 4.1**). The color of dissolved C_{60}:C_{70} is dominated by the C_{70} absorption and hence also appears ruby-red. UV-vis absorption spectra of C_{60}:C_{70} are linear superpositions of the spectra of the individual components (note the isosbestic point at 360 nm), which indicates that C_{60} and C_{70} do not interact in solution.

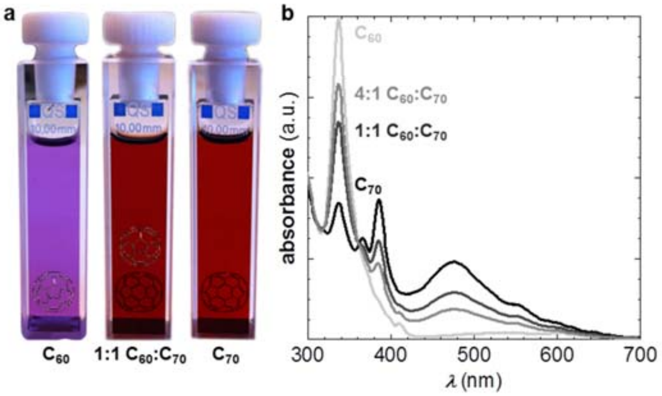

***Figure 4.1 a**) solutions of C_{60}, C_{70} and a 1:1 C_{C60}:C_{70} mixture in o-DCB. **b**) UV-vis absorbance spectra of fullerene solutions in o-DCB with varying C_{70} fraction. (adapted from paper I)*

In order to investigate the solubility behavior of neat fullerenes in more detail, the solubility was determined as a function of C_{60}:C_{70} ratio with *o*-DCB as the solvent (commonly used for lab-scale device processing). The solubility was determined by adding an excess of fullerene material to the solvent, followed by the dissolution of the soluble fraction and careful determination of the concentration after removal of the insoluble fraction by centrifugation. **Figure 4.2a** shows the solubility of C_{60} and C_{70} in o-DCB at 27 ˚C as a function of C_{60}:C_{70} weight ratio (molar ratio), reaching a broad maximum at 54 g L^{-1} for a 1:1 weight ratio. Neat C_{60} and C_{70} feature a lower solubility of 22 and 26 g L^{-1}, respectively. This enhanced solubility can be explained with a higher configurational entropy of the mixture that is obtained upon dissolution compared to neat C_{60} and C_{70}.

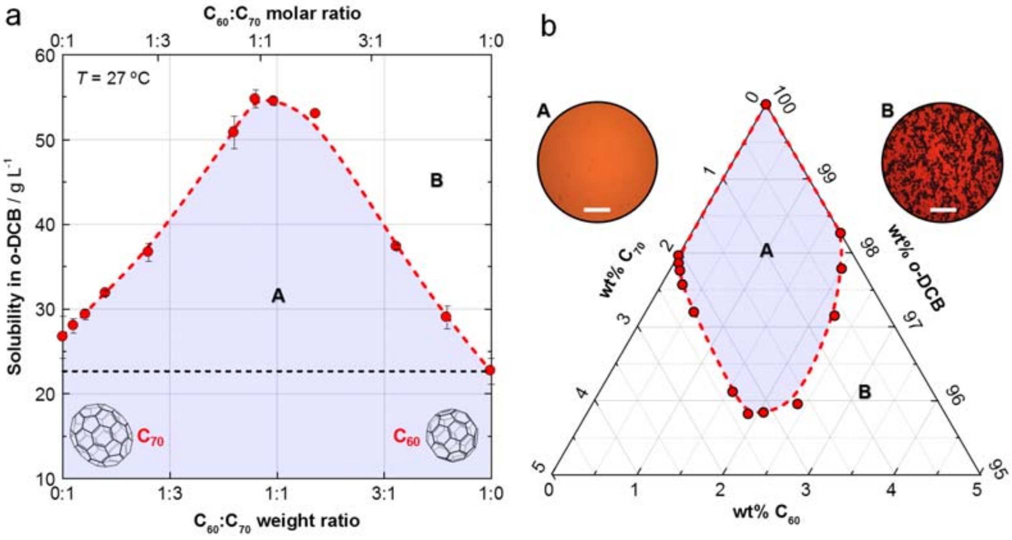

***Figure 4.2 a**) Solubility of C_{60} and C_{70} in o-DCB at 27 ˚C as a function of C_{C60}:C_{70} weight ratio (molar ratio). **b**) Ternary phase diagram of C_{60}:C_{70}:o-DCB at 27 ˚C. (A) represents a single-phase region (blue-shaded area) and (B) a two-phase region; transmission optical images of a 35 g L^{-1}solution of 1:1 C_{60}:C_{70} (top left) and a 60 g L^{-1} solution of 3:1 C_{60}:C_{70} (top right), sandwiched between glass slides (scale bar 300 µm). (adapted from paper II)*

The ternary diagram in **Figure 4.2b** summarizes the solubility-composition dependence of the C_{60}:C_{70}:*o*-DCB system. A single-phase region is observed at concentrations above the liquidus line (homogeneous solutions). Instead, a two-phase region exists at high fullerene concentrations, which corresponds to saturated solutions with aggregates of excess C_{60} and/or C_{70}.

The enhanced entropy of C_{60}:C_{70} mixtures as compared to the entropy of either single fullerene sufficiently reduces the tendency to crystallize (cf. chapter 3), which facilitates film formation during spin coating (9 wt% UHMW-PS was added as a binder material to adjust the viscosity). As can be seen in **Figure 4.3** reference films of neat C_{60} and C_{70} dewet during spin-coating the active layer of field-effect transistors (FETs), whereas C_{60}:C_{70} forms a homogeneous film. [76,79,121]

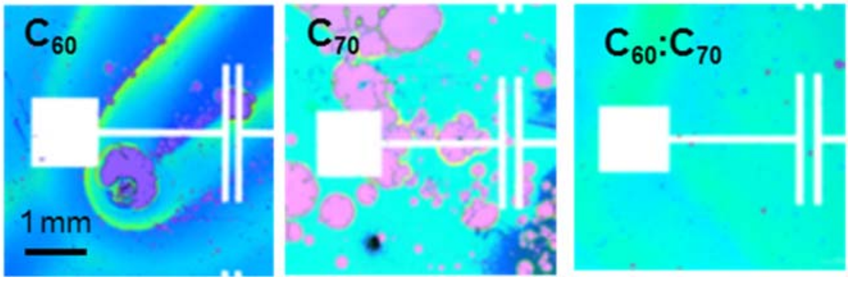

Figure 4.3 *Optical images of neat fullerene films on transistor test substrates. 9 wt% UHMW-PS were added as a binder. (reproduced from paper II)*

4.1.1 Configurational entropy of neat fullerene mixtures

The difference in configurational entropy upon dissolving mixtures of two molecules instead of single components can be derived by using an approach that is similar to the one encountered as part of the Flory-Huggins theory for polymer solutions. Consider a lattice where (1) $N_{solvent}$ solvent molecules occupy one lattice site each, whereas (2) N_{solute} solute molecules occupy the equivalent of r_{solute} lattice sites each. The van der Waals molecular volume of an *o*-DCB molecule is V_{vdW} ~111 Å^3, which is smaller than the volume V_{vdW} ~549 and 646 Å^3 of C_{60} and C_{70}, respectively. Therefore, C_{60} and C_{70} occupy the equivalent of r_{solute} ~5 and 6 lattice sites, whereas *o*-DCB occupies one site. The total number of sites is given by:

$$N = N_{solvent} + r_{solute} N_{solute}$$

The configurational entropy of mixing is then given by:

$$\Delta S_{mix} = -k_B \cdot \left[N_{solvent} \ln \frac{N_{solvent}}{N} + N_{solute} \ln \frac{r_{solute} \cdot N_{solute}}{N} \right]$$

where k_B is the Boltzmann constant.

The volume fractions of the solvent and solute are:

$$\phi_{solvent} = \frac{N_{solvent}}{N}$$

$$\phi_{solute} = \frac{r_{solute} \cdot N_{solute}}{N}$$

where $1 = \phi_{solvent} + \phi_{solute}$.

Now consider binary solutions of either C_{60} or C_{70} in a given amount of solvent:

$$\frac{-\Delta S_{mix}^{C_{60}}}{k_B} = N_{C_{60}} \ln \phi_{C_{60}} + N_{solvent} \ln \phi_{solvent}$$

$$= N_{C_{60}} \ln \phi_{C_{60}} + N \cdot (1 - \phi_{C_{60}}) \cdot \ln(1 - \phi_{C_{60}})$$

$$\frac{-\Delta S_{mix}^{C_{70}}}{k_B} = N_{C_{70}} \ln \phi_{C_{70}} + N_{solvent} \ln \phi_{solvent}$$

$$= N_{C_{70}} \ln \phi_{C_{70}} + N \cdot (1 - \phi_{C_{70}}) \cdot \ln(1 - \phi_{C_{70}})$$

and a ternary solution of C_{60} + C_{70} in the same amount of solvent:

$$\frac{-\Delta S_{mix}^{ternary}}{k_B} = N_{C_{60}} \ln \phi_{C_{60}} + N_{C_{70}} \ln \phi_{C_{70}} + N_{solvent} \ln \phi_{solvent}$$

$$= N_{C_{60}} \ln \phi_{C_{60}} + N_{C_{70}} \ln \phi_{C_{70}} + N \cdot (1 - \phi_{C_{60}} - \phi_{C_{70}}) \cdot \ln(1 - \phi_{C_{60}} - \phi_{C_{70}})$$

One thus obtains the difference in the entropy of mixing between the ternary solution and the two binary solutions as:

$$\Delta \mathrm{S} = \Delta S_{mix}^{ternary} - \Delta S_{mix}^{C_{60}} - \Delta S_{mix}^{C_{70}}$$

$$\frac{-\Delta S}{N k_B} = \left(1 - \phi_{C_{60}} - \phi_{C_{70}}\right) \cdot \ln(1 - \phi_{C_{60}} - \phi_{C_{70}}) - (1 - \phi_{C_{60}}) \cdot \ln(1 - \phi_{C_{60}}) - (1 - \phi_{C_{70}}) \cdot \ln(1 - \phi_{C_{70}})$$

In the dilute solution limit where $\phi_{C_{60}}, \phi_{C_{70}} \approx 0$ we can use the relation $\ln(1 - x) \approx -x$ for small x to obtain a simple relation for the entropy gain upon co-dissolving C_{60} + C_{70} in a common solvent:

$$\frac{-\Delta S}{N k_B} = 2 \cdot \phi_{C_{60}} \cdot \phi_{C_{70}}$$

$$\Delta S \propto \phi_{C_{60}} \cdot \phi_{C_{70}}$$

Which implies that ΔS is maximized if:

$$\boldsymbol{\phi_{C_{60}} = \phi_{C_{70}}}$$

In summary, the maximum entropy gain and hence the highest increase in solubility is achieved if a 1:1 C_{60}:C_{70} *volume* ratio is co-dissolved.

This result suggests that the observed increase in solubility, which occurs at a 1:1 C_{60}:C_{70} ratio, correlates with the highest configurational entropy of ternary solutions (cf. discussion about entropy of mixing in chapter 3 and 6). C-NMR spectroscopy was used to exclude interactions between C_{60} and C_{70} (cf. Paper II).

4.2 TQ1:C_{60}:C_{70} ternaries

In this study, the thiophene-quinoxaline copolymer TQ1 (see the inset of **Figure 4.4b** for chemical structure of TQ1) was used as the electron donor material. TQ1 is an attractive polymer that combines several desirable features such as ease of synthesis,[20] excellent solubility in organic solvents, a narrow bandgap E_g ~ 1.78 nm, a high T_g ~ 100-110 °C,[91,paper III] good photo-stability,[122] and a good photovoltaic performance with a PCE of up to 6-7%.[20,37]

To analyze the nanostructure of spin-coated thin films, atomic force microscopy (AFM), transmission electron microscopy (TEM) and selected area electron diffraction (SAED) were used. TEM was carried out by Olof Bäcke (Dept. of Physics, Chalmers). Tapping mode AFM images suggest a homogeneous surface texture with root mean square (RMS) roughness of only 0.5 nm. In the corresponding TEM bright field images no distinct, phase-separated domains can be seen and SAED patterns reveal only an amorphous halo, indicating that no fullerene crystals have formed (see **Figure 4.4a**). Photoluminescence (PL) measurements indicate that in TQ1:C_{60}:C_{70} films the polymer emission is strongly quenched as evidenced by a large PL quenching ratio Φ ~ 125 (see **Figure 4.4b**). These measurements conclude that TQ1:C_{60}:C_{70} blends are finely mixed.

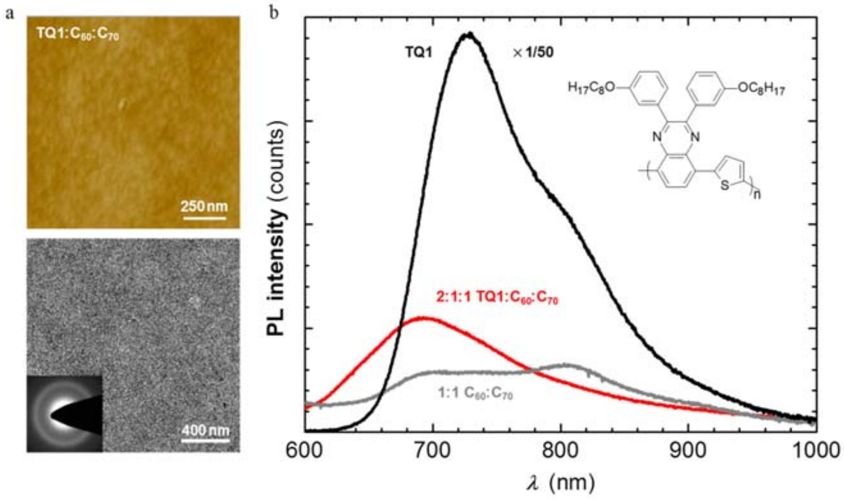

***Figure 4.4** a) AFM height image and TEM bright field image of a 2:1:1 TQ1:C_{60}:C_{70} film; inset: SAED pattern, b) photoluminescence (PL) spectra of a neat TQ1 film (black, signal reduced 50 times), 1:1 C_{60}:C_{70} (grey) and 2:1:1 TQ1:C_{60}:C_{70} (red), inset: chemical structure of TQ1. (reproduced from paper I)*

***Table 3:** Performance of optimized solar cells (average of 3-4 devices on the same substrate, best performance in brackets). (adapted from paper I)*

Blend	**thickness**	***J*$_{sc}$**	***V*$_{oc}$**	***FF***	***PCE***
	(nm)	(mA cm^{-2})	(mV)	(-)	(%)
1:1 TQ1:$PC_{61}BM$	95 ± 5	7.5 ± 0.1	910 ± 3	0.48 ± 0.01	3.4 ± 0.1 (**3.5**)
1:1 TQ1:C_{60}	97± 6	6.6 ± 0.2	810 ± 10	0.48 ± 0.01	2.5 ± 0.1 (**2.6**)
5:4:1 TQ1:C_{60}:C_{70}	131 ± 2	7.2 ± 0.2	770 ± 20	0.46 ± 0.03	2.6 ± 0.2 (**2.8**)
2:1:1 TQ1:C_{60}:C_{70}	96 ± 2	8.4 ± 0.1	780 ± 4	0.54 ± 0.01	3.6 ± 0.1 (**3.7**)
1:1 TQ1:C_{70}	120 ± 2	8.2 ± 0.2	760 ± 3	0.45 ± 0.03	2.9 ± 0.2 (**3.1**)

The photovoltaic performance of TQ1:C_{60} and TQ1:C_{70} binary blends is lower compared to the ternary blends (**see figure 4.5a** and **Table 3**). The use of neat fullerenes slightly reduces the V_{oc} by 0.1-0.15 V compared to devices based on $PC_{61}BM$.[123] Square-wave voltammetry measurements revealed that $PC_{61}BM$ and C_{60} have similar LUMO levels of 4.3 eV. The slightly different V_{oc} may arise due to the formation of neat fullerene aggregates, which are too small to be detected with TEM.

A number of previous studies report that the *FF* of ternary blends is composition dependent, and that the addition of a small amount of a third component to a binary BHJ blend can cause a significant decrease in *FF*.[124,125] However for the case of 2:1:1 TQ1:C_{60}:C_{70} ternary blends the opposite trend is observed, the *FF* increases by ~0.1. At the same time the J_{sc} increases by 1.8 mA cm^{-2} when compared with TQ1:C_{60} solar cells. Besides, the EQE increases by more than 40% at the absorption peak around 580 nm (see **Figure 4.5b**). It should be noted that using a fullerene ratio of 4:1 C_{60}:C_{70}, which is typically obtained from fullerene synthesis,[126,127] gives rise to a lower *FF* in comparison with the 1:1 C_{60}:C_{70} ratio.

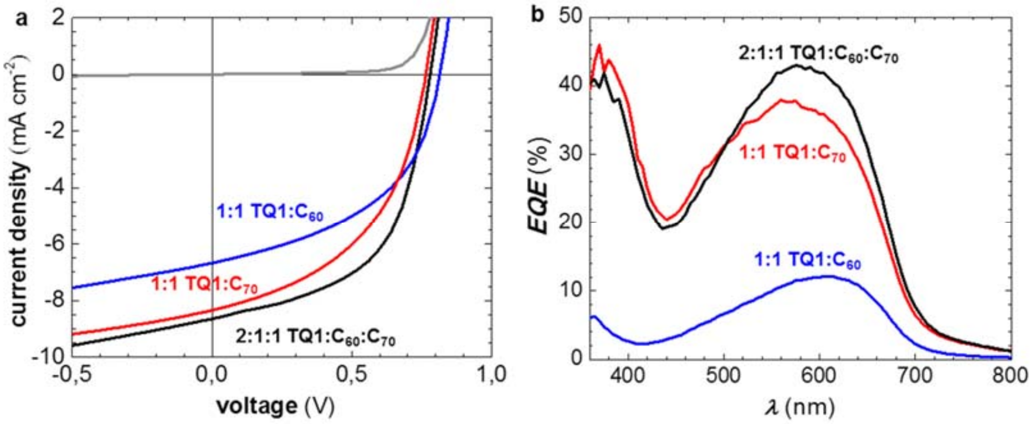

Figure 4.5 *a) IV characteristics and b) EQE spectra of optimized devices based on TQ1:C_{60} (blue), TQ1:C_{70} (red) and 2:1:1 TQ1:C_{60}:C_{70} (black). Note that the EQE of TQ1:C_{60} is much lower due to the device was aged (reproduced from paper I)*

From this study, it can be concluded that the use of neat fullerene mixtures in ternary blends can improve the *FF*, J_{sc} and hence PCE provided that the right fullerene ratio is selected.

4.2.1 PTB7:C_{60}:C_{70} ternaries

The use of neat fullerene mixtures as an electron acceptor material was further investigated by replacing the donor material. The widely studied narrow-bandgap fluorothienobenzodithiophene copolymer PTB7 was selected due to its strong absorption and good photovoltaic performance (see chemical structure in the inset of **Figure 4.6b**).[18,128,129]

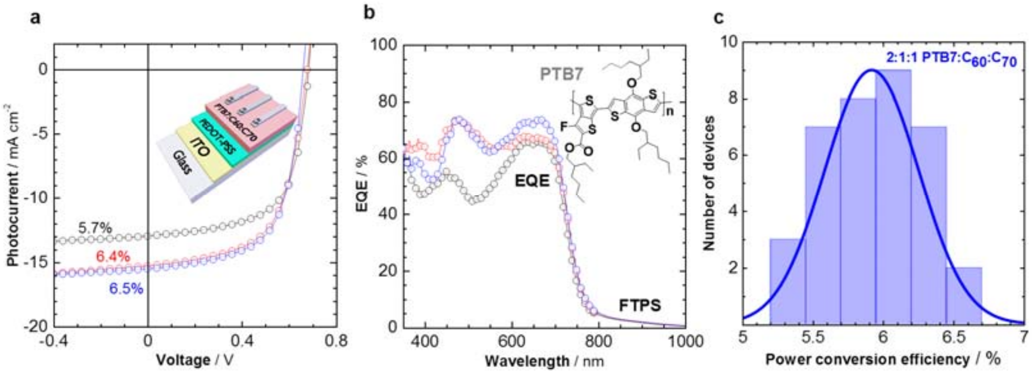

Figure 4.6 *a) IV curves (inset: solar cell device structure) and b) EQE (inset: chemical structure of PTB7) of devices based on PTB7:*C_{60} *(black), PTB7:*C_{70} *(red) and 2:1:1 PTB7:*C_{60}*:*C_{70} *(blue). c) device reproducibility based on 36 PTB7:*C_{60}*:*C_{70} *solar cell devices; the solid line is a Gaussian fit. (reproduced from paper II)*

The ratio of polymer to fullerene mixture was chosen to be 1:1 by weight because for TQ1:C_{60}:C_{70} ternaries equal amounts of donor and acceptor material resulted in the highest power conversion efficiency. PTB7:fullerene photovoltaic devices show a comparable FF and V_{oc} for binary and ternary blends (see **Figure 4.6a** and **Table 4**). Instead, the J_{sc} is more affected by the C_{60}:C_{70} ratio. PTB7:C_{60} binary blends show a lower photocurrent than C_{70}-containing ternary blends, which can be explained by the weaker absorption of C_{60} as compared to C_{70} (see **Figure 4.1b**). This finding was supported by the corresponding EQE spectra (see **Figure 4.6b)**, which confirm that the replacement of C_{60} by C_{70} leads to higher photocurrent generation. A J_{sc} as high as 14.9 mA cm^{-2} is obtained for a 2:1:1 PTB7:C_{60}:C_{70} ternary blend, which is comparable to the J_{sc} of PTB7:PC$_{71}$BM.[128,129] Although PTB7:C_{70} binary devices display a similar PCE, ternary blends are more cost-effective (see **Table 1** in chapter 2), accomplishing the same photovoltaic performance at lower cost.

Similar to the TQ1:fullerene case, the V_{oc} is independent of the fullerene ratio (see **Table 4**). Again, a 0.1 V reduction is observed compared to PCBM-based devices.[128] Overall, the solar cell efficiency of all PTB7:fullerene devices reaches on average 6%, which is the highest value reported to date for devices using pristine fullerenes as the acceptor.

Moreover, excellent reproducibility of the photovoltaic performance was observed. A comparison of all 2:1:1 PTB7:C_{60}:C_{70} devices that were fabricated for this study reveal a narrow standard deviation of ΔPCE ~ ± 0.6 % (**Figure 4.6c**). This is despite the fact that for some devices the concentration of the processing solution and the spin coating speed were varied. Moreover, some active layers were annealed for 10 min at 100 ˚C (see **Table 4**). The thermal stability of PTB7:C_{60}:C_{70} ternaries is further discussed in chapter 5.

Table 4: *Performance of optimized solar cells (best performance in brackets; *annealed for 10 min at 100 ˚C). (adapted from paper II)*

Blend	**Total conc.** / g L^{-1}	**No. of devices**	**Thickness** / nm	J_{sc} / mA cm^{-2}	V_{oc} / mV	***FF*** / -	**PCE** / %
1:1 PTB7:C_{60}	40	6	~ 90	11.9±1.2	668±1	0.61±0.03	4.9±0.6 **(5.7)**
1:1 PTB7:C_{70}	40	6	~ 90	14.6±0.6	664±1	0.62±0.01	6.0±0.3 **(6.4)**
5:4:1 PTB7:C_{60}:C_{70}	40	6	~ 120	14.3±0.6	663±1	0.53±0.01	5.1±0.3 **(5.4)**
2:1:1 PTB7:C_{60}:C_{70}	40	6	~ 150	14.4±0.7	663±1	0.62±0.01	6.0±0.3 **(6.5)**
2:1:1 PTB7:C_{60}:C_{70}	30	24	~ 120	14.9±0.8	660±1	0.60±0.03	5.9±0.6 **(6.5)**
2:1:1 PTB7:C_{60}:C_{70}^{*}	30	6	~ 120	14.1±0.1	663±1	0.62±0.01	5.9±0.3 **(6.2)**

5

5 Thermal stability of ternary blends

5.1 Relevance of the glass transition temperature

To enable commercialization, it is critical to ensure the long-term stability of organic solar cells. Degradation of organic solar cells can have many causes, such as chemical or structural changes of the electrodes, interlayers and/or active layer that occur due to exposure to (UV) light, oxygen, water and elevated temperature, but also delamination and cracking of layers. One important aspect is the thermal stability of the BHJ nanostructure of the active layer during fabrication and operation.

With regard to the manufacture of organic solar cells, the coating speed is limited by the rate of solvent removal, which can be accelerated by heating. The choice of substrate restricts the highest processing temperature. For instance, when PET foil is used as the substrate, the processing temperature is limited to 140 ˚C.[130,131] Instead, substrates made of *e.g.* poly(ethylene naphthalate) (PEN) can endure temperatures up to 180 ˚C.[132] However, PET is a cheaper alternative, and is therefore the most commonly used substrate. Thermal stability of the active layer is also essential for a long lifetime of the solar cells. Industry standards require cycling between -40 ˚C to +85 ˚C, which the active layer must be able to endure.[133]

The nanostructure is not in thermal equilibrium after deposition. Hence, upon annealing during fabrication changes in nanostructure may occur. This can be detrimental for the device performance.[83,134,135] It is therefore recommended to select donor:acceptor blends with a high glass transition temperature in order to prevent reorganization of the nanostructure upon heating.[136] Finely mixed blends usually exhibit a single T_g where the nanostructure stays frozen-in. it is important to note that relaxation of the donor polymer and diffusion of the fullerene acceptor are slowed down but can nevertheless occur on a sufficiently long timescale.

The use of fullerene alloys is a promising approach that permits to enhance the thermal stability below and around the T_g of the blend. Cheng *et al.* have demonstrated that $PC_{61}BM$:$PC_{71}BM$ based solar cells can display a high photovoltaic performance with a PCE above 10% and high thermal stability up to 130 ˚C.[137] Lindqvist *et al.* have studied the thermal stability of a ternary blend based on $PC_{61}BM$:$PC_{71}BM$ and TQ1, and found that the power conversion efficiency deteriorated above 100 ˚C (see Figure 5.1).[79] In Paper III the T_g of this ternary blend was determined with plasmonic nanospectroscopy (*cf.* chapter 3). A T_g~120 ˚C is in agreement with the reported influence of the annealing temperature on the photovoltaic performance of 2:1:1 TQ1:$PC_{61}BM$:$PC_{71}BM$.

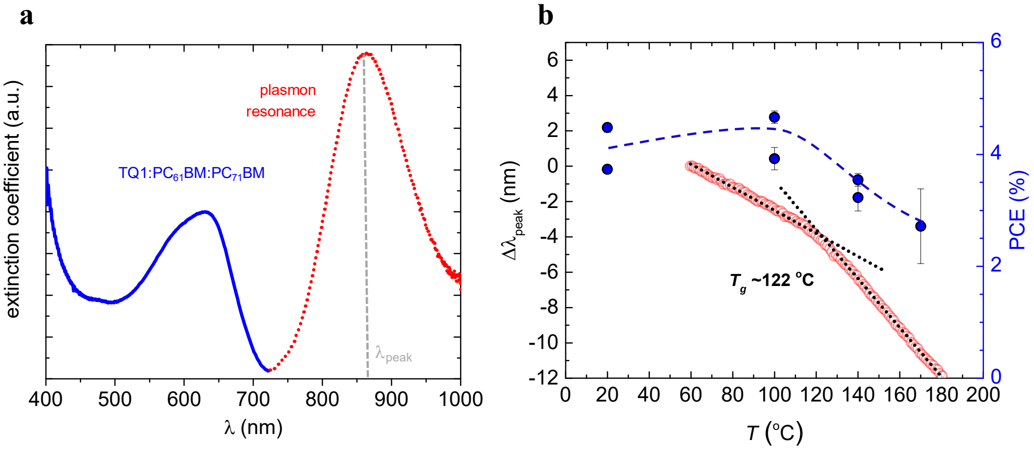

Figure 5.1 *a) Optical absorption of a 5:4:1 TQ1:$PC_{61}BM$:$PC_{71}BM$ thin film (blue) and the localized surface plasmon resonance (LSPR) of the Ag nanodisk sensor (red). b) First plasmonic nanospectroscopy heating scan of 5:4:1 TQ1:$PC_{61}BM$:$PC_{71}BM$ from 60 to 180˚C (red circles) and PCEs from Ref. 79 (blue circles) of 2:1:1 TQ1:$PC_{61}BM$:$PC_{71}BM$. The intersection of the straight lines indicates the glass transition temperature. (reproduced from Paper IV, measurements were carried out by Ferry A.A. Nugroho, Dept. of Physics, Chalmers)*

The remainder of this chapter describes the thermal stability of ternary blends based on neat fullerene mixtures. The use of neat fullerene mixtures is cost effective because several steps associated with the synthesis of PCBMs can be avoided (*cf.* chapter 2). To measure the T_g, plasmonic nanospectroscopy was used. Furthermore, the impact of changes in nanostructure (above T_g) on photovoltaic device performance are discussed (summary of paper IV).

5.2 Glass transition temperature of ternary blends based on neat fullerene alloys

No information about the thermal stability of ternary systems based on neat fullerenes is available in the literature. Therefore, a series of plasmonic nanospectroscopy experiments was carried out. Measurements of C_{60}:C_{70} thin films were not conclusive, likely because of the high transition temperatures that can be anticipated for unsubstituted fullerenes. In contrast, plasmonic nanospectroscopy of ternary blends showed a distinct change in $d(\Delta\lambda_{peak})/dT$, which can be associated with the glass transition (*cf.* chapter 3).

Thin films of 2:1:1 TQ1:C_{60}:C_{70} show a glass transition temperature around 140 ˚C (see **Figure 5.2**), which is higher than the glass transition temperature of neat TQ1,[91] 1:1 TQ1:$PC_{61}BM$,[138] and 2:1:1 TQ1:$PC_{61}BM$:$PC_{71}BM$. **Table 5** summarizes the glass transition temperatures and PCEs of different TQ1:fullerene blends.

Table 5. *Summary of the glass transition temperatures and PCE of TQ1:fullerene blends. n.m. = not measured. Note that two T_gs have been reported for TQ1:$PC_{71}BM$. The strong tendency of this blend to phase-separate during spin-coating leads to a TQ1-rich and $PC_{71}BM$-rich phase that both display a distinct T_g.*[139]

Blend	**T_g (˚C)**	**PCE (%)**	***Ref.***
TQ1:$PC_{61}BM$	110	4.9	[138]
TQ1:$PC_{71}BM$	110/160	7	139, 86, 37
TQ1:$PC_{61}BM$: $PC_{71}BM$	123	4.5	Paper III
TQ1:$PC_{61}BM$:C_{60}	n.m.	3.6	140
TQ1:C_{60}:C_{70}	141	3.6	Paper IV

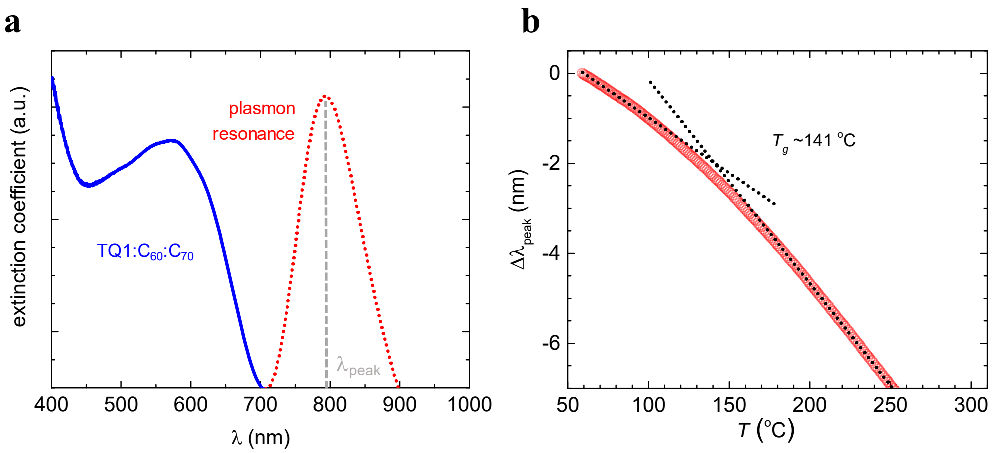

Figure 5.2 *a) Optical absorption of a 2:1:1 TQ1:C_{60}:C_{70} thin film (blue) and the localized surface plasmon resonance (LSPR) of the Au nanodisk sensor (red). b) First plasmonic nanospectroscopy heating scan of 2:1:1 TQ1:C_{60}:C_{70} from 60 to 300 ˚C. Note that the T_g shifts to 182 ˚C during subsequent heating scans. The intersection of the straight lines indicates the glass transition temperature. (reproduced from Paper IV, measurements were carried out by Ferry A.A. Nugroho, Dept. of Physics, Chalmers)*

A second system based on PTB7 and neat fullerenes was studied (paper IV). A 100 nm thin film of a 2:1:1 PTB7:C_{60}:C_{70} blend was deposited on top of a nanoplasmonic sensor array of Au nanodisks (covered with Si_3N_4 support layer), which have a plasmon resonance at λ_{peak} ~920 nm. The NIR resonance was chosen to avoid any overlap with the absorption of the ternary blend (see **Figure 5.3a**).

When heating from 60 to 250 ˚C, there is a continuous blue shift of the plasmon resonance peak $\Delta\lambda_{peak}$ with a change in the slope $d(\Delta\lambda_{peak})/dT$ around 224±1 ˚C, which is attributed to the glass transition temperature of the ternary blend (see **Figure 5.2b** and chapter 3). The onset of change in the slope is located at about 180 ˚C, which indicates that changes in the nanostructure of the blend occur at lower temperatures than the nominal T_g. The high glass transition of the 2:1:1 PTB7:C_{60}:C_{70} ternary blend lies considerably above both, the likely range of processing and operating temperatures.

While such a high T_g is not necessary to render the active layer blend inert when tested on a short timescale, it may nevertheless be of advantage for complete long-term stability. Changes in nanostructure can occur below T_g, provided that the material is given a sufficient amount of time. For instance, Bergqvist *et al.* observed that local changes in nanostructure occur in TQ1:$PC_{61}BM$ when annealed as much as 70 ˚C below the T_g of the blend.[83] The further below T_g a material is annealed, the slower any sub-T_g annealing process will be.

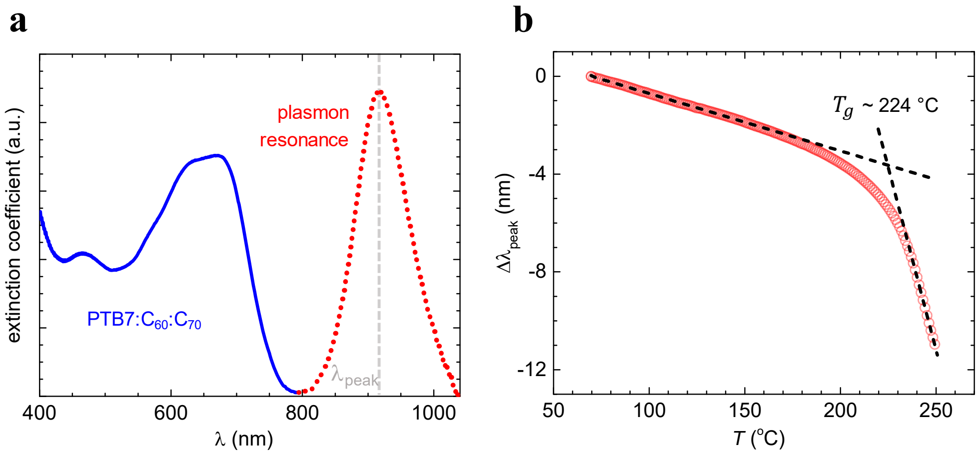

Figure 5.3 *a) Optical absorption of a 2:1:1 PTB7:C_{60}:C_{70} thin film (blue) and the localized surface plasmon resonance (LSPR) of the Au nanodisk sensor (red). b) First plasmonic nanospectroscopy heating scan to monitor the shift in the LSPR peak $\Delta\lambda_{peak}$ during heating from 60 to 250 ˚C (red); the intersection of the straight dashed lines indicates the glass transition temperature. Note that the T_g shifts to ~230 ˚C during subsequent heating scans (reproduced from Paper IV, measurements were carried out by Ferry A.A. Nugroho Dept. of Physics, Chalmers)*

5.3 Evolution of the nanostructure above the glass transition temperature

Annealing of a bulk heterojunction blend above its glass transition temperature can lead to coarsening through liquid-liquid phase-separation and/or crystallization of one or several blend components.[24,136,138] Fullerenes tend to be disordered after solution processing but when annealed form crystals that can reach many micrometers in size. In order to inspect the nanostructure evolution after annealing, transmission electron microscopy (TEM), selected area electron diffraction (SAED) and photoluminescence (PL) spectroscopy were carried out.

Figure 5.4 shows TEM bright field images after heating up to 240 ˚C. Evidently, a fine-grained homogeneous nanostructure is preserved up to an annealing temperature of 180 ˚C, which is supported by the corresponding SAED pattern, showing an amorphous halo. Upon increasing the annealing temperature to 190 ˚C, micrometer-sized, single-crystal-like entities are seen in the TEM images surrounded by a bright halo. This depletion region originates from the diffusion of fullerene material towards the growing crystals. The lower electron density of the remaining PTB7-rich phase gives rise to bright regions that surround the crystals. The depletion region, which manifests itself as a bright halo, has been observed previously around fullerene crystals that have grown in polymer:fullerene BHJ blends.[134,138,141,142]

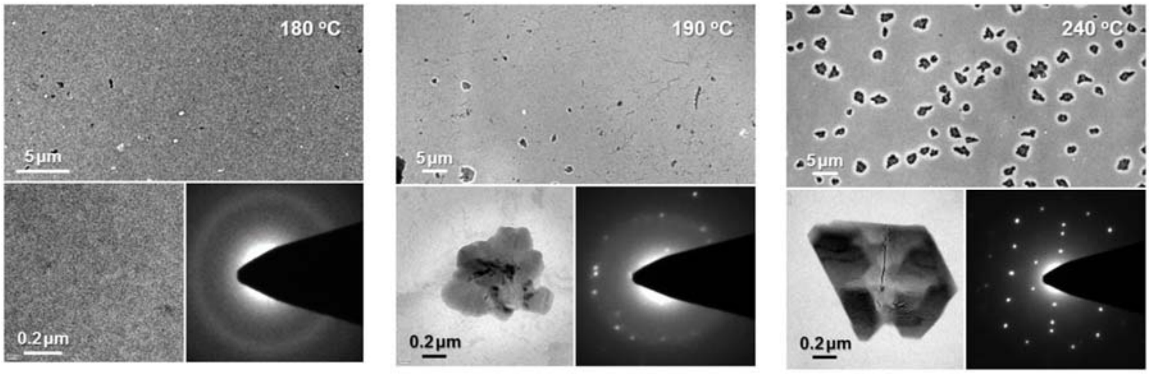

Figure 5.4 *TEM images and electron diffraction patterns (bottom right) of 2:1:1 PTB7:*C_{60}*:*C_{70} *thin films after annealing for 10 min at 180 ˚C (left), 190 ˚C (middle) and 240 ˚C (right). (reproduced from Paper IV, measurements were carried out by Olof Bäcke, Dept. of Physics, Chalmers)*

PL measurements reveal that the emission of neat PTB7 is strongly quenched by a factor of 130 when the fullerene alloy is added (see supporting information of paper IV). The emission remains strongly quenched upon annealing the blend up to 300 ˚C, which indicates that no pure polymer domains have developed.

5.4 Impact of thermal annealing on the photovoltaic performance of PTB7:C_{60}:C_{70}

A series of solar cells was prepared to study the impact of annealing on the photovoltaic performance of 2:1:1 PTB7:C_{60}:C_{70} ternary blends. A 100-110 nm thick active layer was deposited onto PEDOT:PSS/ITO coated glass (see chapter 2.4.2 for device architecture). The active layer was annealed, before top electrode deposition, in the dark for 10 min at T_{anneal} ranging from room temperature to 300 ˚C. For $T_{anneal} \leq 180$ ˚C, the photovoltaic performance is unaffected (no statistically significant change is observed; see **Figure 5.5)**. Upon annealing above this temperature both J_{sc} and FF start to decrease, first slowly up to T_{anneal} ~220 ˚C, which is in agreement with the onset of the glass transition temperature at ~180 ˚C as observed with plasmonic nanospectroscopy (cf. **Figure 5.3b**). The rapid deterioration of the solar cell performance at higher temperatures coincides with the T_g ~224 ˚C.

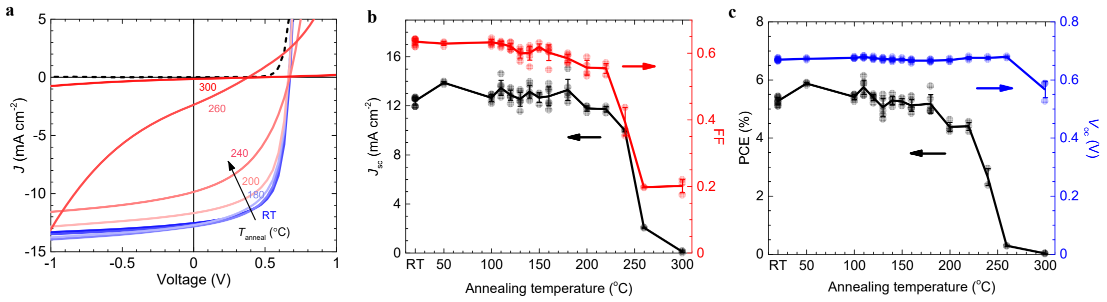

Figure 5.5 *a) current-voltage J-V characteristics of 2:1:1 PTB7:C$_{60}$:C$_{70}$ devices, with active layers thermally treated at T$_{anneal}$, dark current of an as-cast device (dashes), b) J$_{sc}$ and FF, c) V$_{oc}$ and PCE of 2:1:1 PTB7:C$_{60}$:C$_{70}$ devices as function of annealing temperature. Each data point corresponds to a measured device, error bars reflect the standard deviation of 3-5 devices on the same substrate (solid lines are a guide to the eye). (reproduced from Paper IV)*

In summary, the investigated PTB7:C$_{60}$:C$_{70}$ ternary blend displays a high glass transition temperature, T_g ~224 ˚C. TEM images confirmed the tendency of the ternary blend to form glassy, amorphous thin films with a homogeneous nanostructure. PCEs remained unaltered at temperatures up to 180 ˚C, which agrees with the onset of the blend T_g.

6

6 Fullerene-free ternary blends

The replacement of fullerenes with alternative acceptors materials currently receives considerable attention. Candidates that offer a more cost-effective synthesis paired with a higher degree of stability are particularly attractive. Solar cell efficiencies of up to 11% have been reported for fullerene-free D:A binary blends,[143] as well as D:A_1:A_2 ternary blends.[69,116,144–146]

Table 6 summarizes the makeup and photovoltaic performance of selected fullerene-free ternary blends. Baran *et al.* studied ternary blends of several donor polymers including P3HT and PTB7-Th that were combined with mixtures of two acceptor materials: IDTBR and IDFBR (an indacenodithiophene and indenofluorene core with benzothiadiazole and rhodamine groups, respectively). For the P3HT:IDTBR:IDFBR system a detailed analysis of the nanostructure was carried out. The 1:1 P3HT:IDTBR binary blend is characterized by a high degree of order. X-ray scattering reveals both crystalline polymer and acceptor domains. The crystallinity of IDTBR is gradually reduced as an increasing fraction of IDTBR is replaced with IDFBR. For a stoichiometry of 1:0.7:0.3 only few IDTBR crystals remain. At higher IDFBR content the acceptor mixture is vitrified and forms an amorphous phase. At a stoichiometry of 1:0.7:0.3 P3HT:IDTBR:IDFBR a PCE ~ 7.7% was obtained, which is a considerable improvement to P3HT:fullerene systems with a PCE of typically around 4%. Ternary blends of PTB7-Th:IDTBR:IDFBR gave rise to a PCE as high as 11% (see **Figure 6.1**).[69] Yu and coworkers carried out another promising study with a record efficiency of 11%.[144] The combination of a wide-bandgap donor polymer (J52),[147] a medium bandgap acceptor (IT-M),[148] and a low-bandgap acceptor,[149] resulted in a broad absorption spectrum that covered the entire visible and near-infrared region from 750 nm to 1200 nm (see **Figure 6.1**).

Table 6: *Summary of photovoltaic performance of selected D:A$_1$:A$_2$ ternary blends.*

Ternary blends	Ratio	J_{sc} [mA cm^{-2}]	V$_{oc}$ [V]	FF [-]	PCE [%]	Ref.
PC10:IDTBR:IDFBR	1:0.5:0.5	17	1.03	0.6	11	69
PTB7-Th:SF-4PDI:TPE-4PDI	1:0.9:0.1	15	0.86	0.48	6.2	146
PTB7-Th:ITIC:PDI	1:0.3:0.7	18	0.84	0.56	7.1	150
PDBT-T1:SdiPBI-Se:ITIC-Th	1:0.5:0.5	15	0.93	0.7	10.1	151
J52:IT-M:IEICO	1:0.8:0.2	20	0.85	0.67	11.1	144

Perylene diimides (PDIs) are an interesting class of materials that feature a high electron mobility of 10^{-1}-10^{-3} cm^2 V^{-1} s^{-1}, similar to that of many fullerene derivatives. In addition, PDIs offer a large optical extinction coefficient (which for fullerenes is smaller in the visible range), as well as superior photochemical and thermal stability, which makes them a promising alternative to fullerene based acceptors.[152–155] However, planar PDIs have a strong tendency to π-stack in the solid state, which gives rise to micrometer-scale ordered domains that lead to incomplete exciton dissociation.[156] Different approaches have been employed to reduce the π-aggregation, such as the synthesis of dimers or trimers.[157–159] During the last two years, several studies have reported PDI based ternary solar cells, with device efficiencies of up to 10% (see **Table 6 and Figure 6.1**).[146,150,151] These studies conclude that a finely phase-separated blend nanostructure with greatly reduced PDI domain size can be achieved upon mixing of all three components. It can be anticipated that the PDI-based acceptors discussed in Refs. 146 and 151 can only crystallize with great difficulty. It is striking that the neat PDI derivative used in Ref. 150, which on its own readily crystallizes (cf. **Figure 6.5**), inhibits PDI aggreagtion when blended with PTB7-Th and ITIC. Evidently, ternary blends are well suited to induce an amorphous (and possibly glassy) nanostructure.

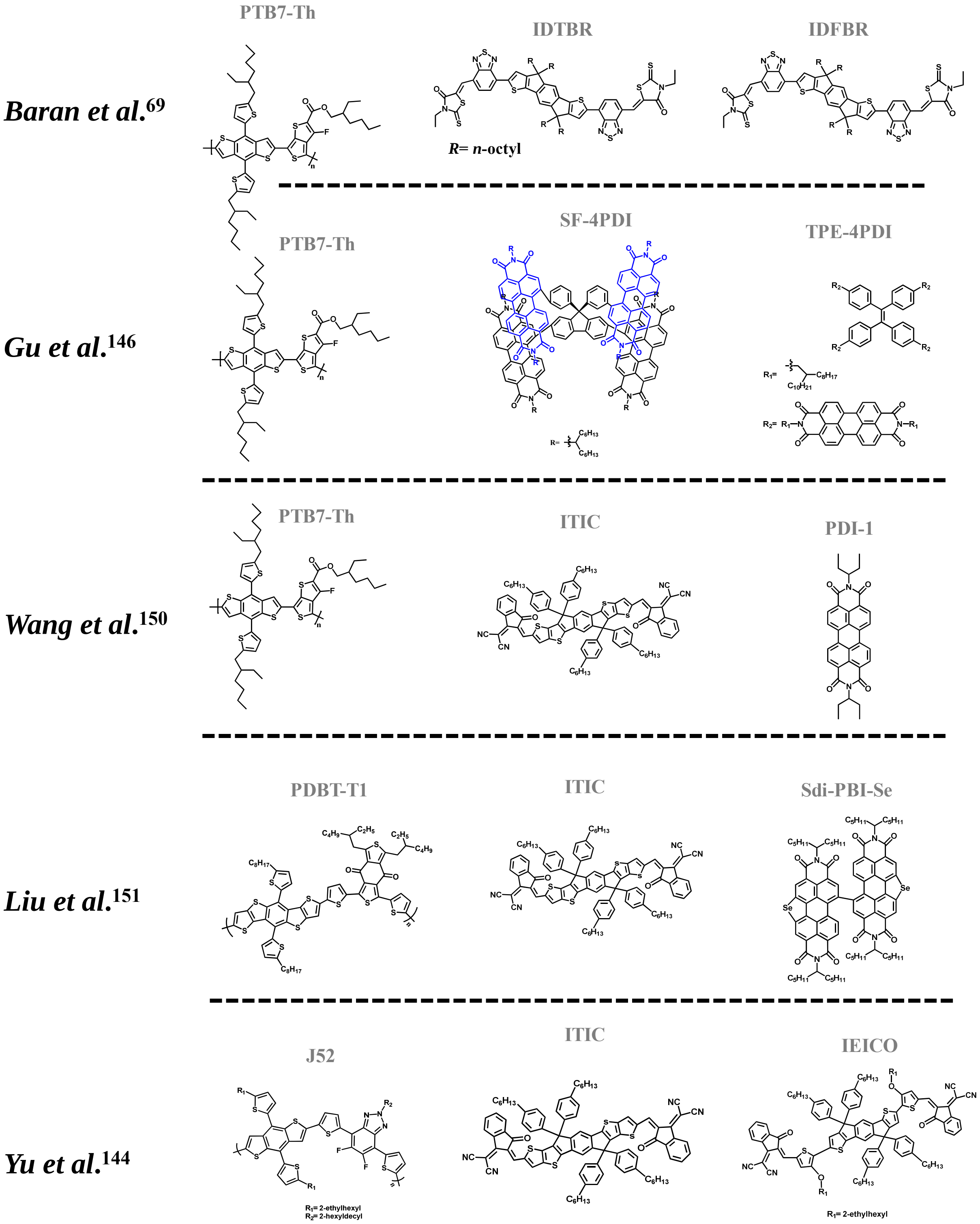

Figure 6.1. *Chemical structure of the donor and acceptor materials used in refs. 69, 146, 150, 151, 144.*

6.1 Solubility of fullerene and non-fullerene mixtures

In chapter 4 the solubility of C_{60}:C_{70} fullerene mixtures was correlated with the composition that is associated with the highest configurational entropy.

The solubility of C_{60}:C_{70} in *o*-DCB and $PC_{61}BM$:$PC_{71}BM$ in CB are compared in **Figure 6.2a,b.** Also in case of $PC_{61}BM$:$PC_{71}BM$, the maximum is located approximately at a 1:1 weight ratio. As discussed in chapter 4, the increase in solubility of mixtures can be explained by the higher configurational entropy of the ternary systems ($PC_{61}BM$:$PC_{71}BM$:*o*-DCB and C_{60}:C_{70}:*o*-DCB), as compared to the corresponding fullerene:solvent binaries.

To explore if the increase in solubility also applies to non-fullerene materials, two additional ternary systems were studied. Rubrene:9,10-diphenylanthracene (DPA) mixtures show the highest solubility at a 1:2 weight ratio, which coincides with the range of compositions that display the highest tendency to vitrify. Vitrification of this mixture was exploited by Stingelin *et al*. to control crystallization in the channel of field effect transistors.[160] Compared with C_{60}:C_{70} mixtures, the maximum solubility of rubrene:DPA is not located at a 1:1 weight ratio, which suggest that besides the configurational entropy of mixing, conformational entropy, and possibly molecular interactions must be taken into account. In the case of PDI-1:PDI-2, which was selected as a potential acceptor mixture, the maximum solubility is located at a 1:1 weight ratio, indicating that the configurational entropy is the most important factor that influences the solubility. The solubility increased upon mixing both PDIs, which suggests that the conclusions drawn in paper I and II also apply to other acceptor mixtures. Similar to C_{60}:C_{70} the solubility increases from about 20 to 50 g L^{-1} in *o*-DCB for a close to equimolar PDI-1:PDI-2 mixture.

Since C_{60}:C_{70}, $PC_{61}BM$:$PC_{71}BM$ and PDI-1:PDI-2 display the highest solubility at a 1:1 stoichiometry it is reasonable to treat these systems as ideal mixtures (cf. eq. 10 and derivation in chapter 4.1.1). It can be anticipated that the entropy of mixing also reduces the crystallization kinetics most strongly for a 1:1 stoichiometry (cf. chapter 3.3). In case of fullerene mixtures complete vitrification is observed. The PDI system, which still crystallizes to some extent, is discussed below. The rubrene:DPA system does not display the highest solubility at a 1:1 stoichiometry and must therefore be treated as a non-ideal solution. However, according to Ref. 160 the highest solubility and tendency for vitrification coincide. The correlation between the increase in solubility and decrease in the rate of crystallization opens up the possibility to use the solubility as a metric to identify potential glass forming mixtures.

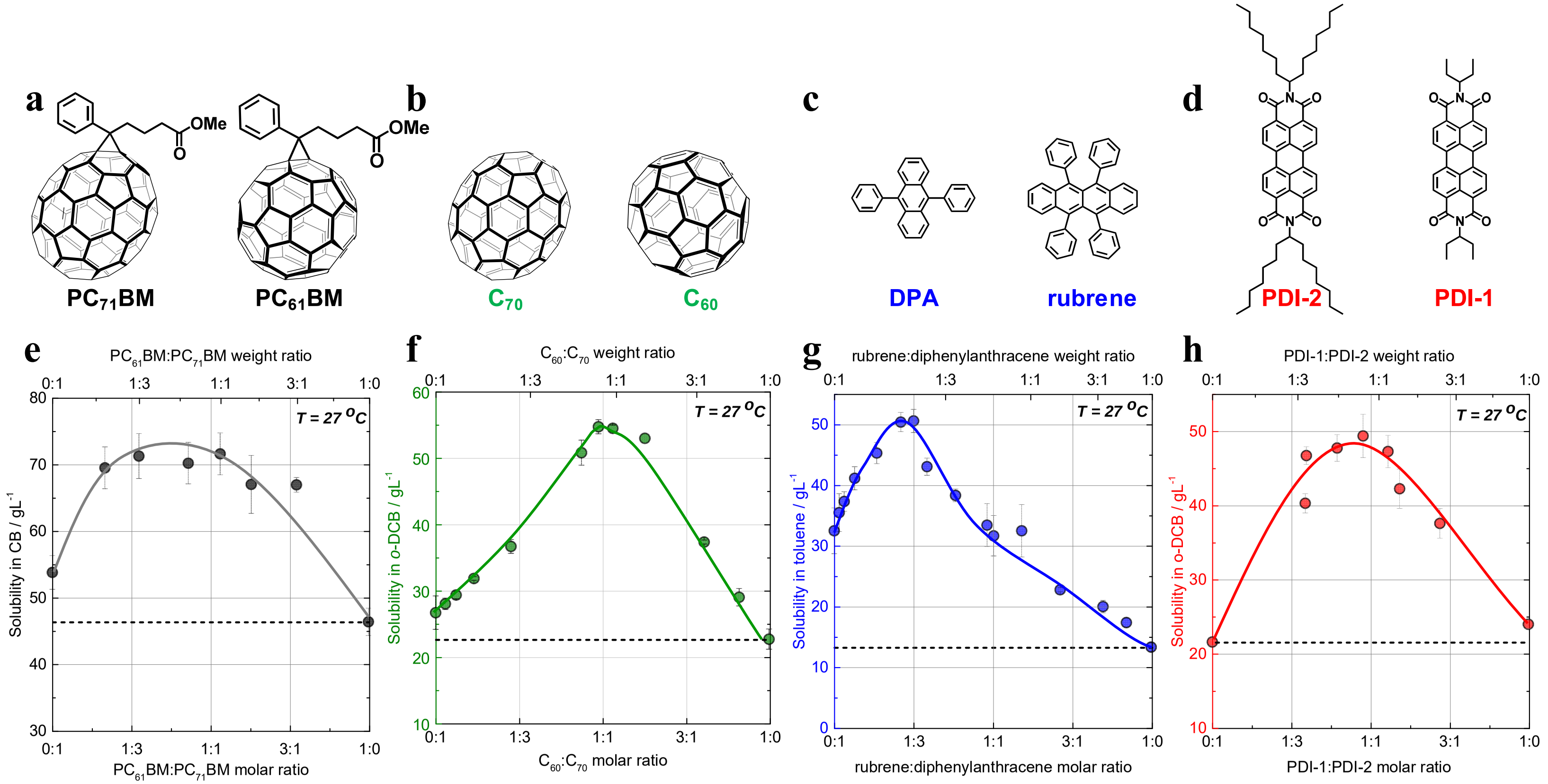

Figure 6.2 *Chemical structures: a) PC$_{71}$BM and PC$_{61}$BM, b) C$_{70}$ and C$_{60}$, c) DPA and rubrene, and d) PDI-2 and PDI-1. Solubility at 27 ˚C of e) PC$_{61}$BM and PC$_{71}$BM in CB, f) C$_{60}$ and C$_{70}$ in o-DCB, g) rubrene and DPA in toluene and h) PDI-1 and PDI-2 in o-DCB as a function of weight ratio (molar ratio). The ratio of PC$_{61}$BM:PC$_{71}$BM, C$_{60}$:C$_{70}$ and rubrene:DPA was determined by reconstructing the UV-vis spectrum recorded for each solute through a linear superposition of reference spectra of separate molecules. The ratio of PDI-1:PDI-2 dissolved in the solvent was determined though Mass Spectrometry. Dashed lines represent the maximum solubility of the less soluble component. Solid lines are a guide to the eye.*

6.2 PTB7:PDI-1:PDI-2 case study

One strategy to reduce the strong tendency for π-stacking of planar PDIs is to use mixtures that aggregate to a lesser extent. In this thesis, a ternary mixture of PTB7, PDI-1 and PDI-2 was studied. PDI-1 and PDI-2 carry different solubilizing branched alkyl substituents that help to reduce aggregation (see **Figure 6.3**) and increase solubility.

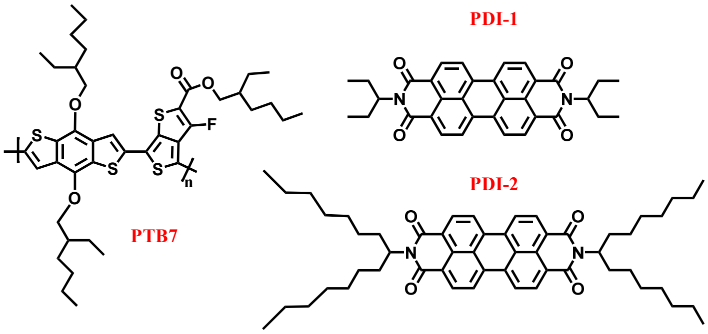

Figure 6.3 *Chemical structures of PTB7, PDI-1 and PDI-2.*

Polarized optical microscopy and AFM images reveal that upon mixing of PTB7 with the two planar PDIs the crystal size is significantly reduced (see **Figure 6.4**). PTB7:PDI-1 and PTB7:PDI-2 show up to ~20 µm and ~5 µm sized crystals, respectively. When adding a second PDI molecule up to ~ 500 nm large crystals form. Organic solar cells were fabricated using PTB7:PDI-1:PDI-2 blends but displayed a too erratic photocurrent to permit any conclusions. The crystal size remains too large for OPV applications.

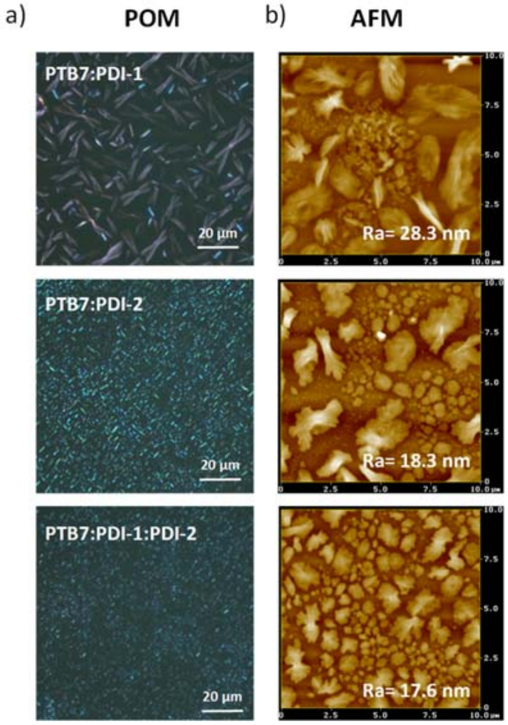

Figure 6.4 *a) Polarized optical microscopy images (POM) of PTB7:PDI-1, PTB7:PDI-2 and PTB7:PDI-1:PDI-2 spin-coated samples on a glass substrate (100×magnification). b) AFM images of spin-coated films of PTB7:PDI-1, PTB7-PDI-2 and PTB7:PDI-1:PDI-2.*

Grazing-Incidence Wide-Angle X-ray Scattering (GIWAXS) was used to further investigate the influence of blending on the microstructure of PTB7:PDIs thin films. Thin films (thickness ~ 100 nm) of PDIs and blends with PTB7 were measured at the D1 beam line of the Cornell High Energy Synchrotron Source (CHESS). Both, PDI-1 and PDI-2 crystallize strongly on their own as indicated by the high diffraction intensities and distinct secondary diffractions (see **Figure 6.5a** and **b**). Upon mixing the PDIs with PTB7, the intensities of the primary diffraction peaks decrease significantly. We note that such reduction is more significant for the PTB7:PDI2 blend (see **Figure 6.5d** and **e**). The ternary blend of PTB7, PDI-1 and PDI-2 (see **Figure 6.5f**) displays a strongly reduced degree of order, which suggests that the use of PDI mixtures is a potential alternative for solution processed solar cells.

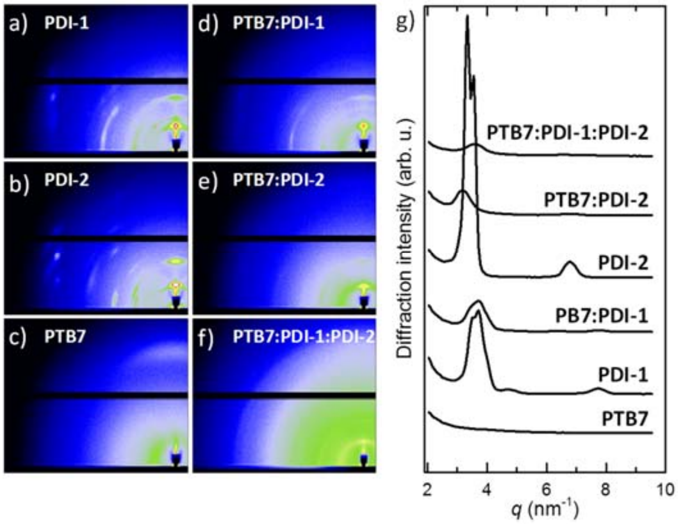

Figure 6.5 *(a-f) Grazing-Incidence Wide-Angle X-ray Scattering (GIWAXS) diffractograms of (a) PDI-1, (b) PDI-2, (c) PTB7, (d) binary blends 1:1 PTB7:PDI-1, (e) 1:1 PTB7:PDI-2 and (f) ternary blend 2:1:1 PTB7:PDI-1:PDI-2. (g) Out-of-plane diffractions based on a-f.*

7

7 Concluding remarks

Organic solar cells are a promising alternative to established solar cell technologies due to their cost-effective production techniques such as large-area printing. High-throughput manufacturing requires thermally stable materials because such a process involves several heating steps during the production. Further, solar cells experience elevated temperatures when exposed to sun light. The use of ternary blends has been the main subject of this thesis. Ternary blends feature a more controlled nanostructure and superior thermal stability of the active layer as compared to binary systems. Most of the work presented in this thesis focuses on bulk-heterojunction blends of the thiophene-quinoxaline polymer TQ1 or the fluorothieno-benzodithiophene polymer PTB7 as the electron donor material and neat fullerene mixtures of C_{60} and C_{70} as the electron acceptor material.

In this thesis, ternary blends were chosen to improve the thermal stability. Neat fullerene mixtures (C_{60} and C_{70}) were used as an acceptor material due to their cost-effectiveness as compared with fullerene derivatives. Solubility studies of C_{60}:C_{70} mixtures revealed enhanced solubility, which was attributed to the higher configurational entropy of C_{60}:C_{70}:solvent ternary solutions, as compared to the C_x:solvent binary solutions. The photovoltaic performance of TQ1:C_{60}:C_{70} and PTB7:C_{60}:C_{70} ternary blends indicates that the use of neat fullerene mixtures is a promising alternative to bulk-heterojunction blends based on PCBMs. Ternary blends of PTB7:C_{60}:C_{70} displayed a highly reproducible power conversion efficiency of 6%, which is a record for devices based on neat fullerenes. Moreover, a high glass transition temperature of 224 ˚C imparts a high degree of thermal stability up to 180 ˚C.

The highly stable glassy nanostructure arises due to alloy formation of C_{60} and C_{70}. Similar to the enhanced solubility in organic solvents, alloy formation benefits from the entropy of mixing. Comparison with other systems, i.e. rubrene:diphenylanthracene, $PC_{61}BM$:$PC_{71}BM$, and two perylene diimide derivatives suggests that the increase in solubility is a common feature. The stoichiometry that displays the highest solubility is thought to also give rise to the highest tendency for glass formation. Finally, recent work on ternary blends based on non-fullerene mixtures was discussed in light of the findings presented in this thesis.

8

8 Outlook

The use of ternary blends, which promises to close the gap between the efficiency, lifetime, and cost requirements needed for commercialization, revives the potential of organic photovoltaics. The findings presented in this thesis are applicable to other donor:acceptor systems and therefore are anticipated to aid the further development of organic photovoltaics. During the last decade, the performance of organic solar cells has strongly increased thanks to advances in synthesis strategies, which together with improved thermal stability of the blend nanostructure may accelerate progress towards large-scale production.

However, the results presented here also open up a number of questions that may serve as motivation for further studies:

- When mixing different molecules to produce ternary solar cells, the interaction between these molecules must be considered to fully understand the solubility enhancement. Further diffusion NMR studies may help to investigate and understand the type of interactions taking place in each system.
- Perylene diimide (PDI) mixtures are a cost-effective material. However, crystallization must be more strongly supressed in order to enable efficient solar cells with these blends. One strategy could be to use a mixture of more than *two* PDI molecules. In this way, each PDI molecule will act as an impurity for the other components, which increases the entropy of mixing and hence tendency for glass formation, leading to an amorphous nanostructure.
- Long-term stability studies of ternary blends will help to understand in more detail how glass formation impacts and extends the lifetime of corresponding solar cells.
- This thesis has introduced the use of neat fullerene alloys to the field of organic photovoltaics. It would be interesting to explore the use of neat fullerene alloys for other applications. For instance, neat fullerenes are of interest for thermoelectrics, due to the very low thermal conductivity that these materials display.[155] Further, recent work has shown the potential of neat fullerene alloys as an interlayer material for perovskite solar cells.[161,162] Finally, as already indicated in paper II, C_{60}:C_{70} alloys permit the fabrication of field-effect transistors with an electron mobility of ~1 cm^2 V^{-1} s^{-1}. This opens up the possibility to fabricate more advanced circuit compounds based on neat fullerene mixtures.

ACKNOWLEDGEMENTS

First and foremost, I would like to express the greatest gratitude to my main supervisor/colleague Christian Müller for accepting to have me as one of his first Ph.D. students at Chalmers. For encouraging me to embrace one of the biggest challenges of my life, in which he has unconditionally guided and supported me. This thesis would not have been possible without your help. I thank you for the constant positive attitude which has helped me to improve and develop personally and professionally.

I would also like to thank Mats Andersson, my "Australian" co-supervisor for all the beneficial discussions. I am grateful to you for letting me be part of your group while I spent a few months 'down under' and for giving me an amazing experience in Adelaide. That was awesome!

During this four and a half years, I had the chance to collaborate with many different groups all over the world. The experience of interacting and working with different groups has inspired me in many ways. I thank all the collaborators that made possible my stay at their respective labs. Mariano Campoy-Quiles from ICMAB-CSIC (Barcelona), Thomas Anthopoulos and Stephan Rossbauer from Imperial College London, Paul Dastoor and Natalie Holmes from Newcastle University (Australia), Koen Vandewal from TU Dresden. I also want to give special thanks to Olle Inganäs and his group at Linköping University. Jonas Bergqvist for the fun and for instructing me on how to make my first solar cells. Armantas Melianas, there are few words that can express how grateful I am for all the help, the inspiring talks and the amazing times we had during conferences. Chalmers collaborators: Eva Olsson, Olof Bäcke, Paul Erhart, Lars Nordstierna, Ferry Nugroho and Christoph Langhammer, thanks for the fun projects!

Frida Andersson and Lotta Pettersson, thanks for making life at our departments easier, fun and enjoyable. You are great! In addition, I would like to thank Anders Mårtensson for spending time teaching me how to use GPC and for being there when a problem popped out.

This time as a Ph.D. student in Sweden has changed me in so many positive ways, most of it thanks to the amazing and unforgettable people I have met. My group, "Müller crew"; You guys are amazing and the experience I had over all these years as a part of a unified and caring group I will never forget. Massi, Mattias, Jonna, Desalegn, Anja, Anna H., Anna

P., Renee, David and Liyang, you guys are amazing. Last but not least, Jason, “el chico”, there is nothing else to say because we have said it all, thanks for being always there for me. I´m going to miss you so much.

To all the former and present colleagues and friends from the 8th floor, THANKS. You made Chalmers unforgettable and unique. A big hug all the way to California to Agi and Tim, we miss you and the time we spent together was priceless. Tina, my friend and best office mate ever, always there for me and always caring, thanks for all cariño.

My Swedish crew, Ambra, Anna P, Anna R, Jason, Ali, Ida and Fanny. Sweden was fun because of you, you all are amazing and made my time here exciting and full of joy!

A esa gente que encontré no hace mucho en el camino y que me han regalado momentos inolvidables, Fatima y Patricia gracias por todo.

Yuri mi amol, tu sí que has sido uno de mis mayores tesoros. No tengo palabras para expresar el cariño que te tengo, aunque a veces me traigas por la calle de la amargura, siempre me sabes hacer feliz con tu pasta que esta teta de monja. Te extraño mucho.

Janis, que puedo decir que ya no te haya dicho. ¡Que me voy a Leuven contigo! ¡Eso es bien!

A mis Vianeses, mi identidad, mi todo; Morenil, Tatito, Txarly, Estela, Esti, Susi, Tanya, Ioar e Izaskunil. Porque parte de esto es gracias a vosotros. Gora zuek! Y no me puedo dejar a mi neska favorita, Zdenka, asko maite zaitudalako, beti elkar.

Todo mi cariño a Los Diaz De Zerio y a Los Mendaza, por que sois un apoyo constante e incondicional.

Amatxu eta Aitatxu, Iker, Lisi eta Enekillo. Vosotros sois la razón de esto. Gracias a vosotros soy lo que soy. Asko maite zaituztet!

Achidi, cariño, you inspire me every single day. Your positivity and constant support is my biggest gift. Thanks for always being there and never letting me down.

REFERENCES

1. http://www.eia.gov/todayinenergy/detail.php?id=12251_20170318.
2. http://www.opec.org/opec_web/en/press_room/3467.htm_20170318.
3. IEA. Energy and Climate Change. *World Energy Outlook Spec. Rep.* 1–200 (2015). doi:10.1038/479267b
4. http://www.iea.org/newsroom/news/2016/november/world-energy-outlook-2016.html_20170318.
5. http://web.unep.org/publications_20170318.
6. http://www.altenergy.org/renewables/solar.html 20170318.
7. Fritts, C. E. On a New Form of Selenium Photocell. *Am. J. Sci.* **26,** 465 (1883).
8. Light-sensitive electric device. *U.S. Pat.* US2,402,66 (1946).
9. Chapin, D. M., Fuller, C. S. & Pearson, G. L. A new silicon p-n junction photocell for converting solar radiation into electrical power [3]. *J. Appl. Phys.* **25,** 676–677 (1954).
10. Sampaio, P. G. V. & González, M. O. A. Photovoltaic solar energy: Conceptual framework. *Renew. Sustain. Energy Rev.* **74,** 590–601 (2017).
11. http://www.nrel.gov_20170318.
12. http://pv.energytrend.com/pricequotes.html_20170523.
13. http://re.jrc.ec.europa.eu/pvgis/cmaps/eur.htm.
14. Shockley, W. & Queisser, H. J. Detailed balance limit of efficiency of p-n junction solar cells. *J. Appl. Phys.* **32,** 510–519 (1961).
15. Kroon, R. *et al.* A new tetracyclic lactam building block for thick, broad-bandgap photovoltaics. *J. Am. Chem. Soc.* **136,** 11578–11581 (2014).
16. Moulé, A. J., Bonekamp, J. B. & Meerholz, K. The effect of active layer thickness and composition on the performance of bulk-heterojunction solar cells. *J. Appl. Phys.* **100,** 94503 (2006).
17. Weinberger, B. R., Akhtar, M. & Gau, S. C. Polyacetylene photovoltaic devices. *Synth. Met.* **4,** 187–197 (1982).
18. Liang, Y. *et al.* For the bright future-bulk heterojunction polymer solar cells with power conversion efficiency of 7.4%. *Adv. Mater.* **22,** 135–138 (2010).
19. Liang, Y. *et al.* Development of New Semiconducting Polymers for High Performance Solar Cells. *J. Am. Chem. Soc.* **131,** 56–57 (2009).
20. Wang, E. *et al.* An easily synthesized blue polymer for high-performance polymer solar cells. *Adv. Mater.* **22,** 5240–5244 (2010).
21. McCullough, R. D. The Chemistry of Conducting Polythiophenes. *Adv. Mater.* **10,** 93–116 (1998).
22. Bao, Z., Dodabalapur, A. & Lovinger, A. J. Soluble and Processable Regioregular poly(3-hexylthiophene) for Thin Film Field-Effect Transistor Applications with High Mobility. *Appl. Phys. Lett.* **69,** 4108 (1996).
23. Havinga, E. E., ten Hoeve, W. & Wynberg, H. A new class of small band gap organic polymer conductors. *Polym. Bull.* **29,** 119–126 (1992).
24. Müller, C. On the glass transition of polymer semiconductors and its impact on polymer solar cell stability. *Chem. Mater.* **27,** 2740–2754 (2015).
25. Diaz De Zerio Mendaza, A. *et al.* High-Entropy Mixtures of Pristine Fullerenes for Solution-Processed Transistors and Solar Cells. *Adv. Mater.* **27,** 7325–7331 (2015).
26. Li, H. *et al.* High-mobility field-effect transistors from large-area solution-grown aligned C60 single crystals. *J. Am. Chem. Soc.* **134,** 2760–2765 (2012).
27. Schilinsky, P., Asawapirom, U., Scherf, U., Biele, M. & Brabec, C. J. Influence of the molecular weight of poly(3-hexylthiophene) on the performance of bulk

heterojunction solar cells. *Chem. Mater.* **17,** 2175–2180 (2005).

28. Müller, C. *et al.* Influence of molecular weight on the performance of organic solar cells based on a fluorene derivative. *Adv. Funct. Mater.* **20,** 2124–2131 (2010).
29. Hoffmann, R., Janiak, C. & Kollmar, C. A chemical approach to the orbitals of organic polymers. *Macromolecules* **24,** 3725–3746 (1991).
30. Kim, Y. *et al.* A strong regioregularity effect in self-organizing conjugated polymer films and high-efficiency polythiophene:fullerene solar cells. *Nat. Mater.* **5,** 197–203 (2006).
31. Dang, M. T., Hirsch, L. & Wantz, G. P3HT:PCBM, Best Seller in Polymer Photovoltaic Research. *Adv. Mater.* **23,** 3597–3602 (2011).
32. Ma, W., Yang, C., Gong, X., Lee, K. & Heeger, A. J. Thermally stable, efficient polymer solar cells with nanoscale control of the interpenetrating network morphology. *Adv. Funct. Mater.* **15,** 1617–1622 (2005).
33. Takacs, C. J., Brady, M. A., Treat, N. D., Kramer, E. J. & Chabinyc, M. L. Quadrites and crossed-chain crystal structures in polymer semiconductors. *Nano Lett.* **14,** 3096–3101 (2014).
34. Verploegen, E. *et al.* Effects of thermal annealing upon the morphology of polymer-fullerene blends. *Adv. Funct. Mater.* **20,** 3519–3529 (2010).
35. Liu, X., Huettner, S., Rong, Z., Sommer, M. & Friend, R. H. Solvent additive control of morphology and crystallization in semiconducting polymer blends. *Adv. Mater.* **24,** 669–674 (2012).
36. Kim, J.-H., Song, C. E., Kang, I.-N., Shin, W. S. & Hwang, D.-H. A highly crystalline low band-gap polymer consisting of perylene and diketopyrrolopyrrole for organic photovoltaic cells. *Chem. Commun. (Camb).* **49,** 3248–50 (2013).
37. Kim, J. Y., Yang, C., Yeom, H. R. & Kim, Y. High-efficiency polymer solar cells with a cost-effective quinoxaline polymer through nanoscale morphology control induced by practical processing additives. *Energy Environ. Sci.* **6,** 1909–1916 (2013).
38. Rossbauer, S., Müller, C. & Anthopoulos, T. D. Comparative study of the N-type doping efficiency in solution-processed fullerenes and fullerene derivatives. *Adv. Funct. Mater.* **24,** 7116–7124 (2014).
39. Wöbkenberg, P. H. *et al.* High mobility n-channel organic field-effect transistors based on soluble C60 and C70 fullerene derivatives. *Synth. Met.* **158,** 468–472 (2008).
40. Anthopoulos, T. D. *et al.* High performance n-channel organic field-effect transistors and ring oscillators based on C60 fullerene films. *Appl. Phys. Lett.* **89,** 2004–2007 (2006).
41. Kroto, H. W., Heath, J. R., O'Brien, S. C., Curl, R. F. & Smalley, R. E. C60: buckminsterfullerene. *Nature* **318,** 162 (1985).
42. A. Hirsch and N. Brettreich. *Fullerenes: Chemistry and Reactions*. (Wiley-VCH Verlag GmbH, Weinheim, 2005).
43. Gharbi, N., Pressac, M., Hadchouel, M., Szwarc, H. & Wilson, S. R. [60] Fullerene is an in vivo Powerful Antioxidant With no Acute or Sub-acute Toxicity. *New York* **5,** 4–7 (2005).
44. Myriam Mellul, L. les R. US5,612,021. (1997).
45. Jarvid, M. *et al.* A new application area for fullerenes: Voltage stabilizers for power cable insulation. *Adv. Mater.* **27,** 897–902 (2015).
46. Liu, Y. *et al.* Aggregation and morphology control enables multiple cases of high-efficiency polymer solar cells. *Nat. Commun.* **5,** 5293 (2014).
47. Yu, G., Gao, J., Hummelen, J. C., Wudl, F. & Heeger, A. J. Polymer Photovoltaic

Cells-Enhanced Efficiencies Via a Network of Internal Donor-Acceptor Heterojunctions. *Science (80-.).* **270,** 1789–1791 (1995).

48. Gasparini, N. *et al.* Neat C70-Based Bulk-Heterojunction Polymer Solar Cells with Excellent Acceptor Dispersion. *Appl. Mater. Interfaces* **6,** 21416–21425 (2014).
49. Lin, H.-W. *et al.* Highly efficient organic solar cells using a solution-processed active layer with a small molecule donor and pristine fullerene. *J. Mater. Chem. A* **2,** 3709 (2014).
50. Tada, K. Solution-processed photocells based on low energy-gap polymer and unmodified C70 composites from halogen-free solvent exceeding 5% power conversion efficiency. *Sol. Energy Mater. Sol. Cells* **143,** 52–57 (2015).
51. Knight, B. W. & Wudl, F. Preparation and Characterization of Fulleroid and Methanofullerene Derivatives. *J. Org. Chem* **60,** 532–538 (1995).
52. Wienk, M. M. *et al.* Efficient methano[70]fullerene/MDMO-PPV bulk heterojunction photovoltaic cells. *Angew. Chem. Int. Ed. Engl.* **42,** 3371–5 (2003).
53. He, Y., Chen, H. Y., Hou, J. & Li, Y. Indene - C60 bisadduct: A new acceptor for high-performance polymer solar cells. *J. Am. Chem. Soc.* **132,** 1377–1382 (2010).
54. Anctil, A., Babbitt, C. W., Raffaelle, R. P. & Landi, B. J. Material and energy intensity of fullerene production. *Environ. Sci. Technol.* **45,** 2353–2359 (2011).
55. Cowan, S. R., Leong, W. L., Banerji, N., Dennler, G. & Heeger, A. J. Identifying a threshold impurity level for organic solar cells: Enhanced first-order recombination via well-defined PC84BM traps in organic bulk heterojunction solar cells. *Adv. Funct. Mater.* **21,** 3083–3092 (2011).
56. Sivaraman, N. *et al.* Solubility of C70 in Organic Solvents. *Fuller. Sci. Technol.* **2,** 233–246 (1994).
57. Beck, M. T. & Mándi, G. Solubility of C60. *Fuller. Sci. Technol.* **5,** 291–310 (1997).
58. Semenov, K. N. *et al.* Solubility of light fullerenes in organic solvents. *J. Chem. Eng. Data* **55,** 13–36 (2010).
59. Doome, R. J., Dermaut, S., Fonseca, A., Hammida, M. & Nagy, J. B. New Evidences for the Anomalous Temperature-Dependent Solubility of C60 and C70 Fullerenes in Various Solvents. *Fuller. Sci. Technol.* **5,** 1593–1606 (1997).
60. Castro, G. & Hornig, J. F. Multiple-Charge-Carrier Generation Processes in Anthracene. *J. Chem. Phys.* **42,** 1459 (1965).
61. Tang, C. W. Two-layer organic photovoltaic cell. *Appl. Phys. Lett.* **48,** 183–185 (1986).
62. Blom, P. W. M., Mihailetchi, V. D., Koster, L. J. A. & Markov, D. E. Device physics of polymer:Fullerene bulk heterojunction solar cells. *Adv. Mater.* **19,** 1551–1566 (2007).
63. Burke, T. M. & McGehee, M. D. How high local charge carrier mobility and an energy cascade in a three-phase bulk heterojunction enable >90% quantum efficiency. *Adv. Mater.* **26,** 1923–1928 (2014).
64. Treat, N. D. *et al.* Polymer-fullerene miscibility: A metric for screening new materials for high-performance organic solar cells. *J. Am. Chem. Soc.* **134,** 15869–15879 (2012).
65. Treat, N. D. *et al.* Interdiffusion of PCBM and P3HT reveals miscibility in a photovoltaically active blend. *Adv. Energy Mater.* **1,** 82–89 (2011).
66. Zhang, F. *et al.* Influence of solvent mixing on the morphology and performance of solar cells based on polyfluorene copolymer/fullerene blends. *Adv. Funct. Mater.* **16,** 667–674 (2006).
67. Lee, J. K. *et al.* Processing additives for improved efficiency from bulk

heterojunction solar cells. *J. Am. Chem. Soc.* **130,** 3619–23 (2008).

68. Müller, C. *et al.* Phase behaviour of liquid-crystalline polymer/fullerene organic photovoltaic blends: thermal stability and miscibility. *J. Mater. Chem.* **21,** 10676 (2011).
69. Baran, D. *et al.* Reducing the efficiency-stability-cost gap of organic photovoltaics with highly efficient and stable small molecule acceptor ternary solar cells. *Nat. Mater.* **84,** 363–370 (2016).
70. Wang, E. *et al.* An isoindigo-based low band gap polymer for efficient polymer solar cells with high photo-voltage. *Chem. Commun.* **47,** 4908 (2011).
71. Benduhn, J. *et al.* Intrinsic non-radiative voltage losses in fullerene-based organic solar cells. *Nat. Energy* **2,** 17053 (2017).
72. Vandewal, K., Tvingstedt, K., Gadisa, A., Inganäs, O. & Manca, J. V. On the origin of the open-circuit voltage of polymer–fullerene solar cells. *Nat. Mater.* **8,** 904–909 (2009).
73. Griffini, G. *et al.* Long-term thermal stability of high-efficiency polymer solar cells based on photocrosslinkable donor-acceptor conjugated polymers. *Adv. Mater.* **23,** 1660–1664 (2011).
74. Carlé, J. E. *et al.* Comparative studies of photochemical cross-linking methods for stabilizing the bulk hetero-junction morphology in polymer solar cells. *J. Mater. Chem.* **22,** 24417 (2012).
75. Yau, C. P. *et al.* Investigation of radical and cationic cross-linking in high-efficiency, low band gap solar cell polymers. *Adv. Energy Mater.* **5,** 1–12 (2015).
76. Angmo, D., Bjerring, M., Nielsen, N. C., Thompson, B. C. & Krebs, F. C. Fullerene alloy formation and the benefits for efficient printing of ternary blend organic solar cells. *J. Mater. Chem. C* **3,** 5541–5548 (2015).
77. Chang, L., Lademann, H. W. A., Bonekamp, J. B., Meerholz, K. & Moulé, A. J. Effect of trace solvent on the morphology of P3HT:PCBM bulk heterojunction solar cells. *Adv. Funct. Mater.* **21,** 1779–1787 (2011).
78. Wong, H. C. *et al.* Morphological stability and performance of polymer-fullerene solar cells under thermal stress: The impact of photoinduced PC60BM oligomerization. *ACS Nano* **8,** 1297–1308 (2014).
79. Lindqvist, C. *et al.* Fullerene mixtures enhance the thermal stability of a non-crystalline polymer solar cell blend. *Appl. Phys. Lett.* **104,** 153301 (2014).
80. Diaz de Zerio Mendaza, A. *et al.* A fullerene alloy based photovoltaic blend with a glass transition temperature above 200 °C. *J. Mater. Chem. A* **5,** 4156–4162 (2017).
81. Campoy-Quiles, M. *et al.* Morphology evolution via self-organization and lateral and vertical diffusion in polymer:fullerene solar cell blends. *Nat. Mater.* **7,** 158–164 (2008).
82. Chem, J. M. *et al.* In situ measurement of power conversion efficiency and molecular ordering during thermal annealing in P3HT:PCBM bulk heterojunction solar cells. *J. Mater. Chem.* **21,** 15224–15231 (2011).
83. Bergqvist, J. *et al.* Sub-glass transition annealing enhances polymer solar cell performance. *J. Mater. Chem. A* **2,** 6146–6152 (2014).
84. Wang, E. *et al.* Conformational disorder enhances solubility and photovoltaic performance of a thiophene-quinoxaline copolymer. *Adv. Energy Mater.* **3,** 806–814 (2013).
85. Papadopoulos, P., Chi, G. F. & Wegner, G. Molecular dynamics of oligofluorenes : A dielectric spectroscopy investigation Molecular dynamics of oligofluorenes : A dielectric spectroscopy investigation. *J. Chem. Phys.* **120,** 2368 (2004).

86. Sharma, A., Pan, X., Campbell, J. A., Andersson, M. R. & Lewis, D. A. Unravelling the Thermomechanical Properties of Bulk Heterojunction Blends in Polymer Solar Cells. *Macromolecules* **50,** 3347–3354 (2017).
87. Xie, R. *et al.* Glass Transition Temperature of Conjugated Polymers by Oscillatory Shear Rheometry. *Macromolecules* **50,** 5146–5154 (2017).
88. Lipomi, D. J. Modelling the morphology and thermomechanical behaviour of low-bandgap conjugated polymers and bulk heterojunction films. *Energy Environ. Sci.* **10,** 558–569 (2017).
89. Campoy-quiles, M., Alonso, M. I., Bradley, D. D. C. & Richter, L. J. Advanced Ellipsometric Characterization of Conjugated Polymer Films. *Adv. Funct. Mater.* **24,** 2116–2134 (2014).
90. Sims, M., Etchegoin, P. G. & Bradley, D. D. C. Thickness-Dependent Thermal Transition Temperatures in Thin Conjugated Polymer Films. *Macromolecules* **39,** 7673–7680 (2006).
91. Kroon, R. *et al.* New quinoxaline and pyridopyrazine-based polymers for solution-processable photovoltaics. *Sol. Energy Mater. Sol. Cells* **105,** 280–286 (2012).
92. Langhammer, C., Larsson, E. M., Kasemo, B. & Zoric, I. Indirect Nanoplasmonic Sensing : Ultrasensitive Experimental Platform for Nanomaterials Science and Optical. *Nano Lett.* **10,** 3529–3538 (2010).
93. Root, S. E., Alkhadra, M. A., Rodriquez, D., Printz, A. D. & Lipomi, D. J. Measuring the Glass Transition Temperature of Conjugated Polymer Films with Ultraviolet − Visible Spectroscopy. **29,** 2646–2654 (2017).
94. Ferenczi, T. A. M. *et al.* Binary Organic Photovoltaic Blends : A Simple Rationale for Optimum Compositions. *Adv. Mater.* **20,** 3510–3515 (2008).
95. Wu, L. *et al.* Ground State Host-Guest Interactions upon Effective Dispersion of Regioregular Poly(3-hexylthiophene) in Poly(9,9-dioctylfluorene-alt-benzothiadiazole). *Macromolecules* **48,** 8765–8772 (2015).
96. Schmelzer, P. Crystal nucleation and growth in glass-forming melts : Experiment and theory. *J. Non. Cryst. Solids* **354,** 269–278 (2008).
97. Yeh, B. J. *et al.* Nanostructured High-Entropy Alloys with Multiple Principal Elements : Novel Alloy Design Concepts and Outcomes. *Adv. Eng. Mater.* **6,** 299–303 (2004).
98. Survey, A. *Organic Light-Emitting Devices*. (2004).
99. Yihong Qiu, Yisheng Chen, Geoff G.Z. Zhang, Lawrence Yu, R. V. M. Developing Solid Oral Dosage Forms: Pharmaceutical Theory and Practice. *Elsevier* (2017).
100. Xu, F., Du, Y., Gao, P., Han, Z. & Chen, G. Influence of quenching rate on the crystallization behaviors of Mg 63 Ni 22 Pr 15 metallic glass. *Mater. Lett.* **61,** 4875–4878 (2007).
101. Zhen, Y. *et al.* Organic solid solution composed of two structurally similar porphyrins for organic solar cells. *J. Am. Chem. Soc.* **137,** 2247–2252 (2015).
102. Hu, Z., Tang, S., Ahlvers, A., Khondaker, S. I. & Gesquiere, A. J. Near-infrared photoresponse sensitization of solvent additive processed poly(3-hexylthiophene)/fullerene solar cells by a low band gap polymer. *Appl. Phys. Lett.* **101,** 53308 (2012).
103. Zhang, M. *et al.* High efficient ternary polymer solar cells based on absorption complementary materials as electron donor. *Sol. Energy Mater. Sol. Cells* **141,** 154–161 (2015).
104. Sun, Q. *et al.* Doping a D-A structural polymer based on benzodithiophene and triazoloquinoxaline for efficiency improvement of ternary solar cells. *Electron.*

Mater. Lett. **11,** 236–240 (2015).

105. An, Q. *et al.* Enhanced performance of polymer solar cells by employing a ternary cascade energy structure. *Phys. Chem. Chem. Phys.* **16,** 16103 (2014).
106. Honda, S., Nogami, T., Ohkita, H., Benten, H. & Ito, S. Improvement of the light-harvesting efficiency in polymer/fullerene bulk heterojunction solar cells by interfacial dye modification. *ACS Appl. Mater. Interfaces* **1,** 804–810 (2009).
107. Hesse, H. C. *et al.* Perylene sensitization of fullerenes for improved performance in organic photovoltaics. *Adv. Energy Mater.* **1,** 861–869 (2011).
108. Leong, W. L., Cowan, S. R. & Heeger, A. J. Differential resistance analysis of charge carrier losses in organic bulk heterojunction solar cells: Observing the transition from bimolecular to trap-assisted recombination and quantifying the order of recombination. *Adv. Energy Mater.* **1,** 517–522 (2011).
109. Huang, T.-Y. *et al.* Efficient ternary bulk heterojunction solar cells based on small molecules only. *J. Mater. Chem. A* **3,** 10512–10518 (2015).
110. Santo, Y., Jeon, I., Sheng Yeo, K., Nakagawa, T. & Matsuo, Y. Mixture of [60] and [70]PCBM giving morphological stability in organic solar cells. *Appl. Phys. Lett.* **103,** 7–11 (2013).
111. Ko, S.-J. *et al.* Improved Performance in Polymer Solar Cells Using Mixed PC61BM/PC71BM Acceptors. *Adv. Energy Mater.* **5,** 1401687 (2015).
112. Zhuo, Z. *et al.* Efficiency improvement of polymer solar cells by iodine doping. *Solid. State. Electron.* **63,** 83–88 (2011).
113. Bonaccorso, F. *et al.* Functionalized Graphene as an Electron-Cascade Acceptor for Air-Processed Organic Ternary Solar Cells. *Adv. Funct. Mater.* **25,** 3870–3880 (2015).
114. Wei, Q., Nishizawa, T., Tajima, K. & Hashimoto, K. Self-organized buffer layers in organic solar cells. *Adv. Mater.* **20,** 2211–2216 (2008).
115. Cheng, Y. J., Hsieh, C. H., Li, P. J. & Hsu, C. S. Morphological stabilization by in situ polymerization of fullerene derivatives leading to efficient, thermally stable organic photovoltaics. *Adv. Funct. Mater.* **21,** 1723–1732 (2011).
116. Khlyabich, P. P., Rudenko, A. E., Thompson, B. C. & Loo, Y. L. Structural Origins for Tunable Open-Circuit Voltage in Ternary-Blend Organic Solar Cells. *Adv. Funct. Mater.* **25,** 5557–5563 (2015).
117. Khlyabich, P. P., Burkhart, B., Rudenko, A. E. & Thompson, B. C. Optimization and simplification of polymer-fullerene solar cells through polymer and active layer design. *Polym. (United Kingdom)* **54,** 5267–5298 (2013).
118. Street, R. A., Davies, D., Khlyabich, P. P., Burkhart, B. & Thompson, B. C. Origin of the tunable open-circuit voltage in ternary blend bulk heterojunction organic solar cells. *J. Am. Chem. Soc.* **135,** 986–989 (2013).
119. Lu, L., Xu, T., Chen, W., Landry, E. S. & Yu, L. Ternary blend polymer solar cells with enhanced power conversion efficiency. *Nat. Photonics* **8,** 716–722 (2014).
120. Liang, Y. *et al.* Highly efficient solar cell polymers developed via fine-tuning of structural and electronic properties. *J. Am. Chem. Soc.* **131,** 7792–9 (2009).
121. Schroeder, B. C. *et al.* Enhancing Fullerene-Based Solar Cell Lifetimes by Addition of a Fullerene Dumbbell. *Angew. Chemie - Int. Ed.* **53,** 12870–12875 (2014).
122. Carlé, J. E. *et al.* Fused thiophene/quinoxaline low band gap polymers for photovoltaics with increased photochemical stability. *Sol. Energy Mater. Sol. Cells* **95,** 3222–3226 (2011).
123. Li, L., Tang, H., Wu, H., Lu, G. & Yang, X. Effects of fullerene solubility on the crystallization of poly(3-hexylthiophene) and performance of photovoltaic devices.

Org. Electron. physics, Mater. Appl. **10,** 1334–1344 (2009).

124. Koppe, M. *et al.* Charge carrier dynamics in a ternary bulk heterojunction system consisting of P3HT, fullerene, and a low bandgap polymer. *Adv. Energy Mater.* **3,** 949–958 (2013).
125. Chen, L., Yao, K. & Chen, Y. Can morphology tailoring based on functionalized fullerene nanostructures improve the performance of organic solar cells? *J. Mater. Chem.* **22,** 18768 (2012).
126. Tsetkova, L. V. *et al.* Extraction of fullerene mixture from fullerene soot with organic solvents. *Russ. J. Gen. Chem.* **81,** 920–926 (2011).
127. Tohji, K. *et al.* Selective and high-yield synthesis of higher fullerenes. *J. Phys. Chem.* **99,** 17785–17788 (1995).
128. Lu, L. & Yu, L. Understanding low bandgap polymer PTB7 and optimizing polymer solar cells based on IT. *Adv. Mater.* **26,** 4413–4430 (2014).
129. Liu, C. *et al.* Single-junction polymer solar cells with over 10% efficiency by a novel two-dimensional donor-acceptor conjugated copolymer. *ACS Appl. Mater. Interfaces* **7,** 4928–4935 (2015).
130. Krebs, F. C. Fabrication and processing of polymer solar cells: A review of printing and coating techniques. *Sol. Energy Mater. Sol. Cells* **93,** 394–412 (2009).
131. Jørgensen, M. *et al.* Stability of polymer solar cells. *Adv. Mater.* **24,** 580–612 (2012).
132. Krebs, F. C. All solution roll-to-roll processed polymer solar cells free from indium-tin-oxide and vacuum coating steps. *Org. Electron.* **10,** 761–768 (2009).
133. Standard Test Methods for Photovoltaic Modules in Cyclic Temperature and Humidity Environments, ASTM Standard E 1171.
134. Bertho, S. *et al.* Influence of thermal ageing on the stability of polymer bulk heterojunction solar cells. *Sol. Energy Mater. Sol. Cells* **91,** 385–389 (2007).
135. Conings, B. *et al.* Modeling the temperature induced degradation kinetics of the short circuit current in organic bulk heterojunction solar cells. *Appl. Phys. Lett.* **96,** 163301 (2010).
136. Bertho, S. *et al.* Effect of temperature on the morphological and photovoltaic stability of bulk heterojunction polymer:fullerene solar cells. *Sol. Energy Mater. Sol. Cells* **92,** 753–760 (2008).
137. Cheng, P. *et al.* Alloy Acceptor: Superior Alternative to PCBM toward Efficient and Stable Organic Solar Cells. *Adv. Mater.* **28,** 8021–8028 (2016).
138. Lindqvist, C. *et al.* Nucleation-limited fullerene crystallisation in a polymer–fullerene bulk-heterojunction blend. *J. Mater. Chem. A* **1,** 7174 (2013).
139. Holmes, N. P. *et al.* Nano-pathways : Bridging the divide between water-processable nanoparticulate and bulk heterojunction organic photovoltaics. *Nano Energy* **19,** 495–510 (2016).
140. Lindqvist, C. *et al.* Fullerene nucleating agents: A route towards thermally stable photovoltaic blends. *Adv. Energy Mater.* **4,** 1301437 (2014).
141. Watts, B., Belcher, W. J., Thomsen, L., Ade, H. & Dastoor, P. C. A quantitative study of PCBM diffusion during annealing of P3HT: PCBM blend films. *Macromolecules* **42,** 8392–8397 (2009).
142. Yang, X., Van Duren, J. K. J., Janssen, R. A. J., Michels, M. A. J. & Loos, J. Morphology and thermal stability of the active layer in poly(p-phenylenevinylene)/methanofullerene plastic photovoltaic devices. *Macromolecules* **37,** 2151–2158 (2004).
143. Hong, S. *et al.* A series connection architecture for large-area organic photovoltaic modules with a 7.5% module efficiency. *Nat. Commun.* **7,** 10279 (2016).

144. Yu, R. *et al.* Two Well-Miscible Acceptors Work as One for Efficient Fullerene-Free Organic Solar Cells. *Adv. Mater.* **29,** 1700437 (2017).
145. Cnops, K. *et al.* 8.4% Efficient Fullerene-Free Organic Solar Cells Exploiting Long-Range Exciton Energy Transfer. *Nat. Commun.* **5,** 3406 (2014).
146. Gu, W. *et al.* Ternary blend polymer solar cells with two non-fullerene acceptors as acceptor alloy. *Dye. Pigment.* **141,** 388–393 (2017).
147. Bin, H. *et al.* Non-Fullerene Polymer Solar Cells Based on Alkylthio and Fluorine Substituted 2D-Conjugated Polymers Reach 9.5% Efficiency. *J. Am. Chem. Soc.* **138,** 4657–4664 (2016).
148. Li, S. *et al.* Energy-Level Modulation of Small-Molecule Electron Acceptors to Achieve over 12% Efficiency in Polymer Solar Cells. *Adv. Mater.* **28,** 9423–9429 (2016).
149. Yao, H. *et al.* Design and Synthesis of a Low Bandgap Small Molecule Acceptor for Efficient Polymer Solar Cells. *Adv. Mater.* **28,** 8283–8287 (2016).
150. Wang, J., Peng, J., Liu, X. & Liang, Z. Efficient and Stable Ternary Organic Solar Cells Based on Two Planar Nonfullerene Acceptors with Tunable Crystallinity and Phase Miscibility. *ACS Appl. Mater. Interfaces* **9,** 20704–20710 (2017).
151. Liu, T. *et al.* Ternary Organic Solar Cells Based on Two Compatible Nonfullerene Acceptors with Power Conversion Efficiency 10%. *Adv. Mater.* **28,** 10008–10015 (2016).
152. Lin, Y. & Zhan, X. Designing efficient non-fullerene acceptors by tailoring extended fused-rings with electron-deficient groups. *Adv. Energy Mater.* **5,** 1501063 (2015).
153. Lin, Y. & Zhan, X. Non-fullerene acceptors for organic photovoltaics: an emerging horizon. *Mater. Horizons* **1,** 470 (2014).
154. McAfee, S. M., Topple, J. M., Hill, I. G. & Welch, G. C. Key components to the recent performance increases of solution processed non-fullerene small molecule acceptors. *J. Mater. Chem. A* **3,** 16393–16408 (2015).
155. Nielsen, C. B., Holliday, S., Chen, H.-Y., Cryer, S. J. & McCulloch, I. Non-Fullerene Electron Acceptors for Use in Organic Solar Cells. *Acc. Chem. Res.* **48,** 2803–2812 (2015).
156. Zhan, X. *et al.* Rylene and related diimides for organic electronics. *Adv. Mater.* **23,** 268–284 (2011).
157. Liang, N. *et al.* Perylene Diimide Trimers Based Bulk Heterojunction Organic Solar Cells with Efficiency over 7%. *Adv. Energy Mater.* **6,** 1600060 (2016).
158. Zhang, X., Zhan, C. & Yao, J. Non-fullerene organic solar cells with 6.1% efficiency through fine-tuning parameters of the film-forming process. *Chem. Mater.* **27,** 166–173 (2015).
159. Shivanna, R. *et al.* Charge generation and transport in efficient organic bulk heterojunction solar cells with a perylene acceptor. *Energy Environ. Sci.* **7,** 435–441 (2014).
160. Stingelin-Stutzmann, N. *et al.* Organic thin-film electronics from vitreous solution-processed rubrene hypereutectics. *Nat. Mater.* **4,** 601–606 (2005).
161. Dai, S. *et al.* Pristine fullerenes mixed by vacuum-free solution process : Ef fi cient electron transport layer for planar perovskite solar cells. *J. Power Sources* **339,** 27–32 (2017).
162. Zhang, K. *et al.* Fullerenes and derivatives as electron transport materials in perovskite solar cells. *Sci. China Chem.* **60,** 144–150 (2017).